Quasi-Binary Transition Metal Dichalcogenide Alloys: Thermodynamic Stability Prediction, Scalable Synthesis and Application

Z. Hemmat[1§], J. Cavin[2§], A. Ahmadiparidari[1], A. Ruckel[3], S. Rastegar[1], S. N. Misal[1], L. Majidi[1], K. Kumar[4], S. Wang[3], J. Guo[3], R. Dawood[3], F. Lagunas[3], P. Parajuli[3], A. T. Ngo[5], L. A. Curtiss[5], S. B. Cho[6], J. Cabana[4], R. F. Klie[3], R. Mishra[5, 7,*], A. Salehi-Khojin[1,*]

[1]Department of Mechanical and Industrial Engineering, University of Illinois at Chicago, Chicago, IL, 60607, USA.

[2]Department of Physics, Washington University in St. Louis, St. Louis, MO 63130, USA.

[3]Department of Physics, University of Illinois at Chicago, Chicago, IL, 60607, USA.

[4]Department of Chemistry, University of Illinois at Chicago, Chicago, IL, 60607, USA.

[5]Materials Science Division, Argonne National Laboratory, Argonne, IL 60439, USA.

[6]Department of Mechanical Engineering and Material Science, Washington University in St. Louis, St. Louis, MO 63130, USA.

[7]Institute of Materials Science and Engineering, Washington University in St. Louis, St. Louis, MO 63130, USA.

[§]These authors contributed equally to this work.

*Corresponding authors. Email: salehikh@uic.edu (A.S.-K); rmishra@wustl.edu (R.M.)

Transition metal dichalcogenide (TMDCs) alloys could provide a wide range of physical and chemical properties, ranging from charge density waves to superconductivity and electrochemical activities. While many exciting behaviors of unary TMDCs have been predicted, the vast compositional space of TMDC alloys has remained largely unexplored due to our lack in understanding of their stability when accommodating different cations or chalcogens in a single-phase. Here, we report a theory-guided synthesis approach to achieve unexplored quasi-binary TMDC alloys through computationally predicted stability maps. We have generated equilibrium temperature-composition phase diagrams using first-principles calculations to identify the stability for 25 quasi-binary TMDC alloys, including those involving non-isovalent cations and verify them experimentally by synthesizing a subset of 12 predicted alloys using a scalable chemical vapor transport method. We demonstrate that the synthesized alloys can be exfoliated into 2D structures, and some of them exhibit: (i) outstanding thermal stability tested up to 1230 K, (ii) exceptionally high electrochemical activity for CO_2 reduction reaction in a kinetically limited regime with near zero overpotential for CO formation, (iii) excellent energy efficiency in a high rate Li-air battery, and (iv) high break-down current density for interconnect applications. This framework can be extended to accelerate the discovery of other TMDC alloys for various applications.

As a class of 2D materials, transition metal dichalcogenides (TMDCs) display diverse physical properties, including topological insulator properties,[1,2] superconductivity,[3–6] valley polarization,[7–10] and enhanced electrocatalytic activity for various chemical reactions.[11–17] This diversity arises due to the ability of TMDCs to accommodate different transition-metal elements, such as Mo, W, V, Nb, Ta, Re and others, with the three chalcogens (S, Se, and Te) in stable

layered structures — that can be exfoliated to a desired number of 2D layers to control quantum confinement. Their properties can be further tuned — or even new properties engineered — by alloying two different elements at either the transition metal or the chalcogen site [18–25] to form quasi-binary alloys, or by simultaneous alloying at both the sites to form quaternary alloys.[17,20,26,27] Thus far, quasi-binary alloys of semiconducting TMDCs, such as $Mo_{(1-x)}W_xS_2$, $Mo_{(1-x)}W_xSe_2$, $MoS_{2(1-x)}Se_{2x}$, and $WS_{2(1-x)}Se_{2x}$, have garnered the most attention as they allow tuning of the band gap.[19,21–25,28–31] In a few other cases, alloying leads to more drastic changes to the crystal structure and electronic properties, for example, the triggering of a metal-to-semiconductor transition by alloying $MoTe_2$ with WTe_2.[32] Theoretical predictions based on first-principles methods provide further impetus for realizing new TMDC alloys by showing the possibility to achieve materials with not only enhanced electronic and optical properties but new properties, such as magnetism.[32–37]

Despite their promise, experimental demonstration of TMDC alloys, especially those involving non-isovalent cations, has been limited. This is primarily due to lack of knowledge regarding the stability of the alloys under relevant growth conditions, which subjects their successful synthesis to a trial-and-error based process. In this work, first-principles density-functional-theory (DFT) calculations were used to evaluate the stability of 25 alloys including monolayer group V and intergroup V and VI transition metal-site TMDC alloys as well as chalcogen-site TMDC alloys with group V and VI transition metals. We attempted growth of a subset of 12 TMDC alloys, performed extensive characterization of the structure and composition of the synthesized materials from microscale to the atomic scale and revealed excellent consistency with the theoretical predictions. The chemical formula of the TM- and chalcogen-site alloys have the form $M_{1-x}M'_xX_2$ and $MX_{2(1-x)}X'_{2x}$, respectively, with $M, M' = \mathrm{Mo, W, V, Nb, Ta}$ and $X, X' = \mathrm{S, Se}$. Table S1 in

Supporting Information lists all the different alloys with a total of 20 TM-site alloys including 2 alloys from group VI, 6 from group V, 12 intergroup of V and VI alloys, as well as 5 chalcogen-site alloys. As all the 10 endmember TMDCs being alloyed are stable in the *2H* phase (see Table S2, Supporting Information), we calculated the stability of all the quasi-binary alloys in the same phase. To verify this assumption, we repeated calculations in the *1T* phase for three example alloys and confirmed that the *2H* phase is the ground state. To discern between miscible alloys — that favor random solid solutions over phase segregation at any temperature — from immiscible ones, we calculated their enthalpy of mixing (ΔH_{mix}). The sign of the mixing enthalpy determines the miscibility of the alloy: negative and positive mixing enthalpies correspond, respectively, to energetically favorable and unfavorable mixing conditions at 0 K. The four group VI TMDC alloys — two TM-site, $Mo_{1-x}W_xS_2$ and $Mo_{1-x}W_xSe_2$, and two chalcogen site, $MoS_{2(1-x)}Se_{2x}$ and $MoS_{2(1-x)}Se_{2x}$ — are known to be miscible, as confirmed in this work.[28,29] In addition, we discovered the four group V quasi-binary alloys, $Nb_{1-x}Ta_xS_2$, $Nb_{1-x}Ta_xSe_2$, $VS_{2(1-x)}Se_{2x}$, and $TaS_{2(1-x)}Se_{2x}$, to be miscible (Figure 1A). The mixing enthalpies of all the alloys are plotted in Figures S1-3, Supporting Information.

For the alloys with positive ΔH_{mix}, synthesis of a single-phase solid solution is still possible. The stability of an alloy is dependent on the change in the free energy of mixing (ΔG_{mix}) as a function of molar concentration. The free energy with respect to the endpoints of an alloy is given by $\Delta G_{mix}(x;T) = \Delta H_{mix}(x) - T\Delta S(x)$. Because entropy ($\Delta S$) is a positive quantity, increasing the temperature causes the free energy to be lowered, stabilizing the alloy (Section S1, Supporting Information). Figure 1B shows the two contributing terms to ΔG, enthalpy ΔH_{mix} and the temperature-dependent $-T\Delta S$ for $W_{1-x}Nb_xS_2$. It is seen that at sufficiently high temperatures, the entropy term dominates, the free energy is reduced, and the alloy is stabilized. Classifying this

temperature-dependent stability requires further analysis of the free energy. For a given finite temperature, the molar concentration of an alloy can be divided into three regions: a stable region, a metastable region, and an unstable region. Figure 1C shows the free energy of $W_{1-x}Nb_xS_2$ at the same temperatures corresponding to Figure 1B. The blue and grey pairs of diamonds demark the boundaries between the stable/metastable regions and metastable/stable regions, respectively (Section S1, Supporting Information). Figure 1D shows the equilibrium phase diagram for $W_{1-x}Nb_xS_2$ with colored lines and grey and blue diamonds that correspond to the temperatures and boundary points displayed in Figure 1C. At ~640 K, the three regions meet, and the alloy is stable at all molar concentrations. This temperature is known as the miscibility temperature. It gives a quantitative metric for the synthesizability of an immiscible alloy. Figure 1E summarizes the miscibility temperatures for all 20 TM-site and 5 chalcogen-site TMDC alloys that we use to predict their formability. The complete equilibrium phase diagrams are shown in Figures S4 and S5, Supporting Information.

To validate the predictions, we have performed alloy synthesis above and below the miscibility temperatures with the expectation that for alloys having a positive ΔH_{mix}, single-phase structures will only be formed above the miscibility temperatures. We selected 9 TM-site and 3 chalcogen-site quasi-binary TMDC alloys for the synthesis. First, $Nb_{1-x}Ta_xS_2$ and $Nb_{1-x}Ta_xSe_2$ which are predicted to be miscible at any temperature and the immiscible alloy of $W_{1-x}Nb_xS_2$ were chosen for the synthesis at two different base temperatures of 500 K and 1300 K. The synthesis process was performed using a scalable chemical vapor transport (CVT) method. The samples were grown with the chemical composition corresponding to $x = 0.5$. During the growth process, by maintaining the temperature gradient between the source (hot zone) and the growth zone (cold zone), we obtained high-quality millimeter-sized crystals at the cold zone and powders with high

crystalline structures at the hot zone. The inset of Figure 2A depicts a typical 1 gram of the powder (e.g. $Nb_{1-x}Ta_xS_2$) collected from the hot zone of ampule which was later used for electrochemical experiments. The synthesized materials were characterized with atomic-resolution scanning transmission electron microscopy (STEM), Raman spectroscopy, X-ray photoelectron spectroscopy (XPS), scanning electron microscopy (SEM), X-ray diffraction (XRD), and energy dispersive X-ray spectroscopy (EDX).

The macroscopic compositions of the synthesized TMDC particles are measured using EDX in an SEM, and the distribution of elemental compositions collected from ~50-60 flakes are shown for $Nb_{1-x}Ta_xS_2$, $Nb_{1-x}Ta_xSe_2$ and $W_{1-x}Nb_xS_2$ at two different synthesis temperatures (Figure 2A, B, and Figures S12-14, Supporting Information). We confirm that the desired stoichiometry of x~0.5 is achieved for $Nb_{1-x}Ta_xS_2$ and $Nb_{1-x}Ta_xSe_2$ at both 500 K and 1300 K, while only the $W_{1-x}Nb_xS_2$ synthesized at 1300 K shows a single-phase averaging x=0.5. When synthesized at 500 K, $W_{1-x}Nb_xS_2$ appears to separate into two endmember phases. This is expected as the predicted miscibility temperature of $W_{1-x}Nb_xS_2$ is ~640 K (Figure 1D). Furthermore, a wider distribution of concentrations is found in the Nb-dense phase compared to the W-dense phase (Figure 2B), consistent with the equilibrium phase diagram of $W_{1-x}Nb_xS_2$, which shows a wider region of stability at 500 K on the Nb-dense side (Figure 1D).

Figure 2C, D show the EDX composition maps for $Nb_{1-x}Ta_xS_2$ and $W_{1-x}Nb_xS_2$, respectively, synthesized at 1300 K, demonstrating that within a single flake, the composition is homogeneous. Atomic-resolution high-angle annular dark-field (HAADF) images from $Nb_{1-x}Ta_xS_2$ and $W_{1-x}Nb_xS_2$, as well as two other alloys of $Mo_{1-x}V_xS_2$ and $MoS_{2(1-x)}Se_{2x}$, are shown in Figure 2E-H. The electron beam diffraction patterns for typical flakes found in the four different TMDCs are shown as insets. The HAADF images and diffraction patterns are obtained for grains

in the [001] orientation. The diffraction patterns are labeled according to 2H phase[38], which is confirmed by the HAADF images for $Nb_{1-x}Ta_xS_2$ and $W_{1-x}Nb_xS_2$. Moreover, we found that the distribution of Nb and Ta (W and Nb) in $Nb_{1-x}Ta_xS_2$ ($W_{1-x}Nb_xS_2$) appears random, as can be seen by the contrast variations in the HAADF images (Figure 2E-F). Since the image contrast in HAADF images depends directly on the average atomic number of the atomic column being imaged, the variation in the atomic column intensity shown in Figure 2E-F is due to the random mixing of both TM elements. We did not find any sign of preferential segregation in either sample. Furthermore, HAADF imaging cannot distinguish between the 1T and 2H phases in the [001] orientation, but the DFT calculations predict that 2H phase has the lowest formation energy, in agreement with the HAADF image analysis.

These results differ from $Mo_{1-x}V_xS_2$ synthesized at 1300 K (Figure 2G). Here, the EDX elemental analysis, electron diffraction and HAADF imaging show clear signs of phase separation towards MoS_2 and VS_2. The electron diffraction pattern (shown as inset in Figure 2G) also suggests a phase segregation. Figure 2G displays a HAADF image of MoS_2 [001] in the 2H phase with 1.2% vanadium doping. This doping causes MoS_2 layers within the 2H $P6_3/mmc$ space group to stack as the 2H $R3m$ phase. Finally, the HAADF imaging and electron diffraction analysis for $MoS_{2(1-x)}Se_{2x}$ shows a homogeneous distribution of Se and S within the sample. Specifically, the HAADF for $MoS_{2(1-x)}Se_{2x}$ [001], as seen in Figure 2H, shows a nearly constant image intensity of the Mo atomic columns, as expected for the 2H $P6_3/mmc$ bulk phase. The electron diffraction patterns and HAADF images were also used to determine the lattice parameters for the $Nb_{1-x}Ta_xS_2$, $W_{1-x}Nb_xS_2$, $Mo_{1-x}V_xS_2$ and $MoS_{2(1-x)}Se_{2x}$ samples (see Table S3, Supporting Information). We note that the lattice parameters for all TMDC alloys analyzed here complies with Vegard's Law,[39] where the lattice parameters of the alloys fall between the two endmembers phases, in excellent

agreement with the theoretical results (see Figure S6, Supporting Information). Our Raman spectroscopy, XPS, and XRD results also confirm the successful synthesis of these materials and verify their chemical compositions, stoichiometric ratios, and crystallinity (Figures S24-26, Supporting Information).

To confirm the theoretical predictions for the rest of the selected materials (8 alloys), we synthesized them at 1300 K. In agreement with the theoretical predictions, we observed homogenous and single-phase structures for $Nb_{1-x}Ta_xSe_2$, $W_{1-x}Nb_xSe_2$, $Mo_{1-x}Nb_xS_2$, $Mo_{1-x}Nb_xSe_2$, $VS_{2(1-x)}Se_{2x}$, $TaS_{2(1-x)}Se_{2x}$, and $V_{1-x}Ta_xS_2$ alloys (Figures S13-21, Supporting Information). In contrast, for the $Mo_{1-x}V_xSe_2$ alloy, EDX and electron diffraction patterns reveal a phase segregated material due to its high miscibility temperature of 1700 K (Figure S23, Supporting Information).

We tested the thermal stability of all synthesized single-phase materials through thermogravimetric analysis (TGA) (Figure 3A). Our results show that $Nb_{1-x}Ta_xS_2$ and $V_{1-x}Ta_xS_2$ retain their structural integrity up to 1230 K with only 3% and 4% weight loss, respectively. At this temperature, $W_{1-x}Nb_xS_2$ shows 10% weight loss while $MoS_{2(1-x)}Se_{2x}$ decomposes completely. All other alloys exhibit 25-50% weight loss and start to melt and decompose at the temperature range of 600-900 K (Figure 3A). Our results shown in Figure 3B indicate that the thermal stability of $Nb_{1-x}Ta_xS_2$ alloy rivals its unary forms, NbS_2 and TaS_2. Moreover, its thermal stability far exceeds that of the commonly used MoS_2 (Figure 3B). NbS_2 and MoS_2 start to melt at ~420K and ~500K, respectively, leaving sulfur vacancies within the structure (Figures S27-31, Supporting Information).

These layered materials in their exfoliated mono- and few-layer forms have great potential to be used in a wide range of applications ranging from nanoelectronics to electrochemical energy conversion and storage systems. To explore the exfoliation capability of the synthesized alloys,

we have utilized both mechanical and liquid-phase exfoliation techniques. For the liquid-phase exfoliation experiments, the alloys $Nb_{1-x}Ta_xS_2$, $Nb_{1-x}Ta_xSe_2$ and $W_{1-x}Nb_xS_2$ were selected (Figure 4A). Details of the exfoliation process are provided in Methods. Dynamic light scattering (DLS) experiments on exfoliated samples show average lateral sizes of ~222 nm, ~199nm, and ~130nm, respectively, for $Nb_{1-x}Ta_xS_2$, $Nb_{1-x}Ta_xSe_2$ and $W_{1-x}Nb_xS_2$ (Figure 4B and Figure S32, Supporting Information). AFM imaging of individual flakes displays typical thicknesses of ~8 to 22 nm for the synthesized NFs (Figure 4C). AFM height profile distributions of the exfoliated materials obtained from ~50 randomly selected exfoliated flakes show a well-controlled thickness with an average of about 15–20 nm (Figure 4D). The work function results for these three alloys are also shown in Figure S33, Supporting Information.

Next, we studied CO_2 reduction performance of exfoliated $Nb_{1-x}Ta_xS_2$, $Nb_{1-x}Ta_xSe_2$ and $W_{1-x}Nb_xS_2$ nanoflakes as cathode materials and found that $Nb_{1-x}Ta_xS_2$ exhibits the highest activity among tested materials. Its activity is also much higher than that of MoS_2 nanoflakes, as one of the most active catalysts for CO_2 reduction reaction.[12,40] We performed linear sweep voltammetry (LSV) experiments in CO_2 saturated 1 M choline chloride and 1 M KOH solution in a three-electrode setup.[15] Figure 4E shows the LSV results at a very low scan rate of 1 mV s^{-1} (kinetically limited regime) for $Nb_{1-x}Ta_xS_2$ and MoS_2 nanoflakes coated on the gas diffusion layer. The results show a remarkably high current density at -0.8 V vs RHE for $Nb_{1-x}Ta_xS_2$ (-273 mA cm^{-2}), far exceeding that of MoS_2 (-104 mA cm^{-2}). At -0.8 V vs RHE, the obtained current densities for $Nb_{1-x}Ta_xSe_2$ and $W_{1-x}Nb_xS_2$ were -192 mA cm^{-2} and -153 mA cm^{-2}, respectively (Figure S34, Supporting Information). Gas-phase products were analyzed in real-time using differential electrochemical mass spectroscopy (DEMS). DEMS results verify that these catalysts are selective towards CO formation rather than H_2 production in the potential window of -0.115 to -0.8 V vs

RHE. The onset potential for CO production was found to be -0.115 V vs RHE for $Nb_{1-x}Ta_xS_2$ suggesting a near zero overpotential of 5 mV, which is the smallest overpotential reported for CO_2 reduction so far (Figure 4F).[12,40]

We also examined the catalytic performance of $Nb_{1-x}Ta_xS_2$ in a lithium-air battery system during the discharge and charging processes. Experiments were carried out in a typical Swagelok-type battery cell. The battery consists of a lithium chip as the anode, a glass fiber separator, an electrolyte and $Nb_{1-x}Ta_xS_2$ nanoflakes coated on a gas diffusion layer as the cathode (see Methods). The electrolyte consists of 0.1 M Lithium Bis (Trifluoromethanesulfonyl) Imide (LiTFSI) as the lithium salt and 0.025 M Indium Iodide (InI_3) as a redox mediator in dimethyl sulfoxide (DMSO) solvent. The battery was operated in a dry air environment at a fixed capacity of 1000 mAh/g with a high rate of 1000 mA/g. As shown in Figure 4G, the first discharge and charge curves are observed at ~2.7V and 3.5V, respectively. Throughout the battery's operation, there is no change in charge potential while surprisingly, the discharge curve gets closer to ~2.8 V and approaches the equilibrium voltage (2.96V). This indicates an efficient reduction and evolution of oxygen corresponding to the formation and decomposition of Li_2O_2 products (Figures S35 and S36, Supporting Information) during discharging and charging, respectively. We note that the $Nb_{1-x}Ta_xS_2$ catalyst shows a very stable performance in the presence of the redox mediator without any evidence of reduction of triiodides to iodides. Thus, the Li_2O_2 capacity loss was found to be negligible in this battery. The ~0.7 V polarization gap is one of the smallest values reported so far for Li-air battery systems.

Motivated by the outstanding thermal stability of $Nb_{1-x}Ta_xS_2$, we also investigated the electrical properties of $Nb_{1-x}Ta_xS_2$ for electronic applications. For this purpose, mechanically exfoliated few-layer $Nb_{1-x}Ta_xS_2$ flakes were transferred onto a SiO_2/Si (~300 nm/0.5 mm) substrate (Figure S37,

Supporting Information) and source-drain regions were patterned by electron beam lithography (EBL). Contact metal electrode of Cr/Au (5/50 nm) was deposited followed by standard nanofabrication process (Section S13, Supporting Information). The current-voltage (I_{DS}-V_{DS}) transport characteristics of the tested devices were found to be linear around zero, implying a good Ohmic contact for the channel of the device. The increasing trend of the resistance with increasing temperature verifies the metallic behavior of this material. Also, we observed negligible gate dependency in transfer characteristics (I–V_G) of the tested devices (Figure S38, Supporting Information). Figure 4H represents the breakdown current density versus voltage characteristics of the $Nb_{1-x}Ta_xS_2$ devices measured at 300 K. It is found that $Nb_{1-x}Ta_xS_2$ devices can withstand very high current densities approaching 40 MA.cm^{-2}, far larger than typical values reported for the commonly used Cu or Al interconnects (<10 MA.cm^{-2}).[41,42] The current density of our multi-layered $Nb_{1-x}Ta_xS_2$ (6-20 nm) is among the highest found in multi-layered nanomaterials such as TiS_3 nanoribbon (1.7 MA.cm^{-2})[43] and multilayer MoS_2 (<1 MA.cm^{-2}).[44] It is also comparable with the current density of multi-layered graphene (~40-60 MA.cm^{-2}).[43] The limit of current densities for $Nb_{1-x}Ta_xS_2$ devices can be significantly increased by employing encapsulation of the material,[42,45] sandwiched structures,[45] and fabrication of small nanoribbon structures.[42,46] With the growing promise of layered materials, the higher current density and thermal stability of $Nb_{1-x}Ta_xS_2$, make it a promising material for high-power electrical interconnects. The (opto)-electronic and electrochemical properties of the other synthesized TMDC alloys remain to be explored in future.

In summary, we report results of a joint-theoretical and experimental study on the synthesis of unexplored quasi-binary TMDC alloys with guidance from theoretically predicted stability maps. It is found that certain materials within this grouping exhibit outstanding thermal stability,

electrochemical, and electrical properties. Future research will explore other emerging properties of these materials, including superconductivity, magnetic and topological insulator behavior. This study opens up an exciting opportunity to probe the chemical and physical characteristics of other quasi-binary TMDCs and accelerate the discovery of multinary TMDC alloys for various high impact applications.

Experimental Section

Chemical Vapor Transport (CVT) of TMDC alloys: Before the reaction, quartz ampoules were thoroughly cleaned using diluted HF to remove any organic surface contaminants. We then rinsed the quartz ampoules several times with distilled water and annealed them at 1300 K for 5 h. The cleaning process for the quartz is necessary as it removes any contamination which interferes with the quality of the crystal. High-purity powders of the transition metals and chalcogens (>99.99% trace metals basis) were mixed in desired stoichiometric proportions and sealed under high vacuum ($<10^{-5}$ torr) in the ampules. The sealed quartz (with an internal diameter of ≈ 10 mm and length of ≈15 cm) were placed into a two-zone tube furnace system for the vapor transport growth. To examine the phase stability behavior of the binary alloys, samples were synthesized at two different base growth temperature of 500 K and 1300 K. During the high-temperature growth synthesis, both zones of the furnace were heated up to 1300 K with the rate of 50 K/h. A temperature gradient was established by setting the source material zone (T_{hot}) at 1300 K and the growth zone (T_{cold}) at 1250 K. The system was maintained at this temperature for one week and then gradually cooled down to room temperature at a 50 K/h rate. However, for the low-temperature growth synthesis, after heating the furnace to 1300 K, the temperature of the hot zone and cold zone were quenched to 500 and 450 K, respectively. The samples were left at this constant temperature for one week and then gradually cooled down to room temperature at a 50 K/h rate.

Computational Details: Disordered alloys were studied using 6×6 supercells of the primitive cell of 2*H*-phase TMDCs with molar concentration $x = 0.25, 0.50,$ and 0.75. Additional x values were used for particularly asymmetric alloys and for the four new stable alloys: $Nb_{1-x}Ta_xS_2$, $Nb_{1-x}Ta_xSe_2$, $VS_{2(1-x)}Se_{2x}$, and $TaS_{2(1-x)}Se_{2x}$. To simulate random alloys within small supercells, we used special quasi-random structures (SQS's).[47] The SQS's were generated using the Alloy Theoretic Automated Toolkit (ATAT).[48] A vacuum spacing of >15 Å was used to reduce the interaction between image planes due to the use of periodic boundary conditions. Total energies were calculated using density-functional theory (DFT) as implemented in VASP using the Perdew-Burke-Ernzerhof exchange-correlation functional.[49,50] For the large SQS's, geometric relaxation was conducted at only the Γ-point in reciprocal space. A subsequent static calculation for the electronic structure was performed using a Γ-centered $3 \times 3 \times 1$ *k*-points mesh generated using the Monkhorst-Pack method.[51] Pure TMDCs were studied using a *k*-points grid of $8 \times 8 \times 1$ for geometry optimization and $24 \times 24 \times 1$ for static calculations. A kinetic energy cutoff of 450 eV was used for all the calculations.

Generating Phase Diagrams: For each alloy, enthalpy values were computed at multiple molar concentration values. These values were fitted to a subregular solution model corresponding to a

cubic fit. The change in entropy due to mixing was assumed to be solely from configurational entropy. With functional forms of the enthalpy and entropy, the change in Gibbs free energy was used to determine the boundaries between the different regions of stability at a grid of temperature values, generating an equilibrium phase diagram. See Section S1 in Supporting Information for more details.

Characterization techniques: The atomic-resolution scanning transmission electron microscopy (STEM) data was acquired using the aberration-corrected JEOl ARM200CF which is a 200 kV STEM/TEM, equipped with a cold-field emission gun. The high-angle annular dark-field (HAADF) images were acquired using a probe size of 0.078 nm, a convergence semi-angle of 23 mrad, and a collection semi-angle from 68 to 175 mrad.

Scanning Electron Microscopy (SEM) characterization was carried out using the Raith e-LiNE plus ultra-high-resolution electron beam lithography (EBL) system. Imaging was performed on the cathode by an acceleration voltage (EHT) of 12 kV.

The SEM-EDX measurements were performed with FEI Quanta 650 ESEM integrated with the Oxford AZtec EDS and EBSD systems. The data were obtained in high vacuum with excellent beam stability.

Thermogravimetric analysis (TGA) tests were performed using a TA TGA Q5000 instrument. Samples were loaded onto a platinum high-temperature pan. A heating rate of 25 K/min was chosen for all specimens, and the temperature range was chosen from room temperature to 1230 K. The nitrogen flow rates for sample and balance were 10 and 25 mL/min, respectively.

Raman data were obtained with a HORIBA LabRAM HR Evolution confocal Raman microscope equipped with a Horiba Andor detector and 532 nm laser source for excitation. The instrument was configured with a laser spot diameter of ~1.3 μm, the objective of 50× at laser intensities of less than 7.5 $\mu W\ \mu m^{-2}$. The measurements were performed at room temperature and ambient conditions.

Ultraviolet Photoelectron Spectroscopy (UPS) and X-ray photoelectron spectroscopy (XPS) data were obtained using a Thermo Scientific ESCALAB 250Xi instrument under high vacuum ($<2\times10^{-8}$ mbar). The high-sensitive XPS system was equipped with an electron flood gun and scanning ion gun. Analysis and peak fitting for each element's data was carried out using the Thermo Avantage software.

X-ray diffraction (XRD) was conducted on a Bruker D8 Advance (40 kV, 40 mA) using a Cu Kα (λavg= 1.5418 Å). The diffraction pattern was recorded from 10 to 75° (2θ).

Dynamic Light Scattering (DLS) measurements were performed using the Malvern Zetasizer Nano ZLS 380 system equilibrated at 25 °C for 60 s. The instrument equipped with a 10 mW, 633 nm semiconductor laser.

Atomic force microscopy (AFM) topography images were obtained using Bruker Dimension Icon AFM with ScanAsyst-air in tapping mode.

Synthesis of TMDC alloy nano-flakes (NFs): TMDC nanoflakes (NFs) were synthesized using a liquid-phase exfoliation method in isopropyl alcohol (IPA) solvent. A mixture of 300 mg of the powder (TMDC alloy) was dispersed in 60 mL IPA solution. The sonication was carried out for

30 h using a probe sonicator (Vibra Cell Sonics 130 W). The resultant dispersions were then centrifuged at high speed (2000 rpm) for 1 h to achieve a supernatant of atomically thin flakes. After centrifugation, the supernatant (roughly the top 70% of the centrifuged solution) was collected for further experiments.

Electrochemical CO_2 reduction experiment: 1 M choline chloride/1 M KOH was used as the electrolyte for the electrochemical reduction of CO_2. The solution was purged with CO_2 until it was saturated (pH ≈ 7.60). Linear sweep voltammetry (LSV) experiments were performed at the scan rate of 1 mV s^{-1}. Tested materials were coated on the gas diffusion layer and were used as working electrodes. Ag/Ag^+ and platinum wire (surface area 0.48 cm^2) were used as reference and counter electrodes, respectively. Potentials were converted to RHE using:

$$V \text{ vs RHE} = V \text{ vs } Ag/Ag^+ + 0.155 + 0.0592 * pH.$$

The reported potentials were iR corrected. Gas products from CO_2 reduction were analyzed in real-time using differential electrochemical mass spectroscopy (DEMS) purchased from Hiden Analytical.

Li-Air Battery experiment: The cathode for the battery experiment was prepared by coating $Nb_{1-x}Ta_xS_2$ nanoflakes on the surface of the gas diffusion layer and the anode, lithium chips (>99.9%), purchased from Sigma-Aldrich. The set-up was assembled in an Ar-filled glove box. The amount of electrolyte immersed in GF/C glass fiber separator was 40 μL. The cycling experiments were carried out by using a potentiostat (MTI- Corporation) with the current density of 1000 mA/g reaching to 1000 mAh/g capacity.

Electrical measurements: To prevent ambient degradation, the $Nb_{1-x}Ta_xS_2$ devices were quickly loaded in a cryogenic probe station under high vacuum environment (chamber pressure = 10^{-8} to 10^{-7} Torr) for electrical measurements. Keithley 2612A System Source Meter was used for applying power to test the Current-voltage (I_{DS}-V_{DS}) characteristics of different test structures.

Data and materials availability: All data needed to evaluate the conclusions in the paper are present in the paper or the Supporting Information.

Acknowledgements

The work of A.S.-K., R.F.K., Z.H., A.A.-P., A.R., S.W., J.G, R.D., F.L., and P.P. are supported by the National Science Foundation DMREF Grant 1729420. A.S.-K., A.T.N, S.R., and L.C acknowledge the support by the U.S. Department of Energy, Office of Energy Efficiency and Renewable Energy, Vehicle Technologies Office. A.S.-K., J.C., K.K, S.N.M. and L.M. acknowledge the support by the National Science Foundation Grant 1800357. J.C., S.B.C., and R.M. acknowledge support through NSF DMREF-1729787. This work used computational resources of the Extreme Science and Engineering Discovery Environment (XSEDE), which is supported by NSF ACI-1548562. The authors acknowledge the use of the Nanotechnology Core Facility and Electron Microscopy Core of UIC's Research Resources Center. This work made use of the Pritzker Nanofabrication Facility at the University of Chicago and the EPIC and Keck-II facility of Northwestern University's NUANCE Center (DMR-1720139 and NSF ECCS-1542205). The authors thank Dr. Fengyuan Shi for her help with imaging, and TEM-EDS data acquisition.

Author contributions: A.S.-K. led the material synthesis and electrochemical/thermal/electronic experiments. R.M. led the computational studies. R.F.K. led the microscopy characterizations. Z.H and A.A.-P. synthesized the TMDC alloys. J.C. and S.B.C. carried out computational studies. Z.H. performed EDX, Raman, and SEM characterizations. A.A.-P. performed TGA. S.R., S.N.M., Z.H., and L.M. performed the electrochemical experiments. Z.H. and S.W. performed AFM, device nanofabrication and electrical measurements. K.K performed XRD. L.M. carried out XPS and DLS experiments. A.R., J.G, P.P., R.D., and F.L. performed the (S)TEM characterization. L.A.C., A.T.N, S.R. and A.S.-K. conceived the idea for the chemistry of Li-air battery system. All authors contributed to the write up of the manuscript.

Conflict of Interest: The authors declare no competing interests.

Keywords:

phase diagrams, transition metal dichalcogenides, alloys, thermal stability, CO_2 reduction, density functional theory.

References

[1] E. Sajadi, T. Palomaki, Z. Fei, W. Zhao, P. Bement, C. Olsen, S. Luescher, X. Xu, J. A. Folk, D. H. Cobden, *Science* **2018**, *362*, 922 LP.

[2] X. Qian, J. Liu, L. Fu, J. Li, *Science* **2014**, *346*, 1344 LP.

[3] Y. Saito, T. Nojima, Y. Iwasa, *Nat. Rev. Mater.* **2016**, *2*, 1.

[4] C. H. Sharma, A. P. Surendran, S. S. Varma, M. Thalakulam, *Commun. Phys.* **2018**, *1*, 90.

[5] E. Navarro-Moratalla, J. O. Island, S. Mañas-Valero, E. Pinilla-Cienfuegos, A. Castellanos-Gomez, J. Quereda, G. Rubio-Bollinger, L. Chirolli, J. A. Silva-Guillén, N. Agraït, G. A. Steele, F. Guinea, H. S. J. van der Zant, E. Coronado, *Nat. Commun.* **2016**, *7*, 11043.

[6] X. Xi, Z. Wang, W. Zhao, J.-H. Park, K. T. Law, H. Berger, L. Forró, J. Shan, K. F. Mak, *Nat. Phys.* **2015**, *12*, 139.

[7] P. Nagler, M. V Ballottin, A. A. Mitioglu, F. Mooshammer, N. Paradiso, C. Strunk, R. Huber, A. Chernikov, P. C. M. Christianen, C. Schüller, T. Korn, *Nat. Commun.* **2017**, *8*, 1551.

[8] K. F. Mak, K. He, J. Shan, T. F. Heinz, *Nat. Nanotechnol.* **2012**, *7*, 494.

[9] A. Arora, R. Schmidt, R. Schneider, M. R. Molas, I. Breslavetz, M. Potemski, R. Bratschitsch, *Nano Lett.* **2016**, *16*, 3624.

[10] H. Zeng, J. Dai, W. Yao, D. Xiao, X. Cui, *Nat. Nanotechnol.* **2012**, *7*, 490.

[11] M. Asadi, B. Sayahpour, P. Abbasi, A. T. Ngo, K. Karis, J. R. Jokisaari, C. Liu, B. Narayanan, M. Gerard, P. Yasaei, X. Hu, A. Mukherjee, K. C. Lau, R. S. Assary, F. Khalili-Araghi, R. F. Klie, L. A. Curtiss, A. Salehi-Khojin, *Nature* **2018**, *555*, 502.

[12] M. Asadi, K. Kim, C. Liu, A. V. Addepalli, P. Abbasi, P. Yasaei, P. Phillips, A.

Behranginia, J. M. Cerrato, R. Haasch, P. Zapol, B. Kumar, R. F. Klie, J. Abiade, L. A. Curtiss, A. Salehi-Khojin, *Science* **2016**, *353*, 467 LP.

[13] P. Abbasi, M. Asadi, C. Liu, S. Sharifi-Asl, B. Sayahpour, A. Behranginia, P. Zapol, R. Shahbazian-Yassar, L. A. Curtiss, A. Salehi-Khojin, *ACS Nano* **2017**, *11*, 453.

[14] L. Majidi, P. Yasaei, R. E. Warburton, S. Fuladi, J. Cavin, X. Hu, Z. Hemmat, S. B. Cho, P. Abbasi, M. Vörös, L. Cheng, B. Sayahpour, I. L. Bolotin, P. Zapol, J. Greeley, R. F. Klie, R. Mishra, F. Khalili-Araghi, L. A. Curtiss, A. Salehi-Khojin, *Adv. Mater.* **2019**, *31*, 1804453.

[15] M. Asadi, M. H. Motevaselian, A. Moradzadeh, L. Majidi, M. Esmaeilirad, T. V. Sun, C. Liu, R. Bose, P. Abbasi, P. Zapol, A. P. Khodadoust, L. A. Curtiss, N. R. Aluru, A. Salehi-Khojin, *Adv. Energy Mater.* **2019**, *9*, 1803536.

[16] Q. Gong, L. Cheng, C. Liu, M. Zhang, Q. Feng, H. Ye, M. Zeng, L. Xie, Z. Liu, Y. Li, *ACS Catal.* **2015**, *5*, 2213.

[17] Q. Gong, S. Sheng, H. Ye, N. Han, L. Cheng, Y. Li, *Part. Part. Syst. Charact.* **2016**, *33*, 576.

[18] H. Li, X. X. Duan, X. Wu, X. Zhuang, H. Zhou, Q. Zhang, X. Zhu, W. Hu, P. Ren, P. Guo, L. Ma, X. Fan, X. Wang, J. Xu, A. Pan, X. X. Duan, *J. Am. Chem. Soc.* **2014**, *136*, 3756.

[19] J. Zhang, S. Jia, I. Kholmanov, L. Dong, D. Er, W. Chen, H. Guo, Z. Jin, V. B. Shenoy, L. Shi, J. Lou, *ACS Nano* **2017**, *11*, 8192.

[20] J. Zhou, J. Lin, X. Huang, Y. Zhou, Y. Chen, J. Xia, H. Wang, Y. Xie, H. Yu, J. Lei, D. Wu, F. Liu, Q. Fu, Q. Zeng, C.-H. Hsu, C. Yang, L. Lu, T. Yu, Z. Shen, H. Lin, B. I. Yakobson, Q. Liu, K. Suenaga, G. Liu, Z. Liu, *Nature* **2018**, *556*, 355.

[21] V. Klee, E. Preciado, D. Barroso, A. E. Nguyen, C. Lee, K. J. Erickson, M. Triplett, B. Davis, I. H. Lu, S. Bobek, J. McKinley, J. P. Martinez, J. Mann, A. A. Talin, L. Bartels, F. Léonard, *Nano Lett.* **2015**, *15*, 2612.

[22] G. Wang, C. Robert, A. Suslu, B. Chen, S. Yang, S. Alamdari, I. C. Gerber, T. Amand, X. Marie, S. Tongay, B. Urbaszek, *Nat. Commun.* **2015**, *6*, 10110.

[23] A. Y. Lu, H. Zhu, J. Xiao, C. P. Chuu, Y. Han, M. H. Chiu, C. C. Cheng, C. W. Yang, K. H. Wei, Y. Yang, Y. Wang, D. Sokaras, D. Nordlund, P. Yang, D. A. Muller, M. Y. Chou, X. Zhang, L. J. Li, *Nat. Nanotechnol.* **2017**, *12*, 744.

[24] Y. Chen, J. Xi, D. O. Dumcenco, Z. Liu, K. Suenaga, D. Wang, Z. Shuai, Y.-S. Huang, L. Xie, *ACS Nano* **2013**, *7*, 4610.

[25] Y. Gong, Z. Liu, A. R. Lupini, G. Shi, J. Lin, S. Najmaei, Z. Lin, A. L. Elías, A. Berkdemir, G. You, H. Terrones, M. Terrones, R. Vajtai, S. T. Pantelides, S. J. Pennycook, J. Lou, W. Zhou, P. M. Ajayan, *Nano Lett.* **2014**, *14*, 442.

[26] S. Susarla, J. A. Hachtel, X. Yang, A. Kutana, A. Apte, Z. Jin, R. Vajtai, J. C. Idrobo, J. Lou, B. I. Yakobson, C. S. Tiwary, P. M. Ajayan, *Adv. Mater.* **2018**, *1804218*, 1.

[27] O. El-Atwani, N. Li, M. Li, A. Devaraj, J. K. S. Baldwin, M. M. Schneider, D. Sobieraj, J.

S. Wróbel, D. Nguyen-Manh, S. A. Maloy, E. Martinez, *Sci. Adv.* **2019**, *5*, eaav2002.

[28] J. Kang, S. Tongay, J. Li, J. Wu, *J. Appl. Phys.* **2013**, *113*, 143703.

[29] H.-P. Komsa, A. V Krasheninnikov, *J. Phys. Chem. Lett.* **2012**, *3*, 3652.

[30] S. Tongay, D. S. Narang, J. Kang, W. Fan, C. Ko, A. V. Luce, K. X. Wang, J. Suh, K. D. Patel, V. M. Pathak, J. Li, J. Wu, *Appl. Phys. Lett.* **2014**, *104*, 012101.

[31] M. Zhang, J. Wu, Y. Zhu, D. O. Dumcenco, J. Hong, N. Mao, S. Deng, Y. Chen, Y. Yang, C. Jin, S. H. Chaki, Y.-S. Huang, J. Zhang, L. Xie, *ACS Nano* **2014**, *8*, 7130.

[32] F. Raffone, C. Ataca, J. C. Grossman, G. Cicero, *J. Phys. Chem. Lett.* **2016**, *7*, 2304.

[33] K. Ikeura, H. Sakai, M. S. Bahramy, S. Ishiwata, *APL Mater.* **2015**, *3*, 41514.

[34] P. Yu, J. Lin, L. Sun, Q. L. Le, X. Yu, G. Gao, C.-H. Hsu, D. Wu, T.-R. Chang, Q. Zeng, F. Liu, Q. J. Wang, H.-T. Jeng, H. Lin, A. Trampert, Z. Shen, K. Suenaga, Z. Liu, *Adv. Mater.* **2017**, *29*, 1603991.

[35] Y. Li, K.-A. N. Duerloo, K. Wauson, E. J. Reed, *Nat. Commun.* **2016**, *7*, 10671.

[36] R. Mishra, W. Zhou, S. J. Pennycook, S. T. Pantelides, J.-C. Idrobo, *Phys. Rev. B* **2013**, *88*, 144409.

[37] Y. C. Cheng, Z. Y. Zhu, W. B. Mi, Z. B. Guo, U. Schwingenschlögl, *Phys. Rev. B* **2013**, *87*, 100401.

[38] P. M. Williams, in (Ed.: F. Lévy), Springer Netherlands, Dordrecht, **1976**, pp. 51–92.

[39] A. R. Denton, N. W. Ashcroft, *Phys. Rev. A* **1991**, *43*, 3161.

[40] M. Asadi, B. Kumar, A. Behranginia, B. A. Rosen, A. Baskin, N. Repnin, D. Pisasale, P. Phillips, W. Zhu, R. Haasch, R. F. Klie, P. Král, J. Abiade, A. Salehi-Khojin, *Nat. Commun.* **2014**, *5*, 4470.

[41] I. Ames, F. M. d'Heurle, R. E. Horstmann, *IBM J. Res. Dev.* **1970**, *14*, 461.

[42] M. J. Mleczko, R. L. Xu, K. Okabe, H.-H. H. Kuo, I. R. Fisher, H.-S. P. Wong, Y. Nishi, E. Pop, *ACS Nano* **2016**, *10*, 7507.

[43] A. J. Molina-Mendoza, J. O. Island, W. S. Paz, J. M. Clamagirand, J. R. Ares, E. Flores, F. Leardini, C. Sánchez, N. Agraït, G. Rubio-Bollinger, H. S. J. van der Zant, I. J. Ferrer, J. J. Palacios, A. Castellanos-Gomez, *Adv. Funct. Mater.* **2017**, *27*, 1.

[44] R. Yang, Z. Wang, P. X.-L. Feng, *Nanoscale* **2014**, *6*, 12383.

[45] J. W. Huang, C. Pan, S. Tran, B. Cheng, K. Watanabe, T. Taniguchi, C. N. Lau, M. Bockrath, *Nano Lett.* **2015**, *15*, 6836.

[46] A. Behnam, A. S. Lyons, M. H. Bae, E. K. Chow, S. Islam, C. M. Neumann, E. Pop, *Nano Lett.* **2012**, *12*, 4424.

[47] A. Zunger, S.-H. Wei, L. G. Ferreira, J. E. Bernard, *Phys. Rev. Lett.* **1990**, *65*, 353.

[48] A. van de Walle, M. Asta, G. Ceder, *Calphad* **2002**, *26*, 539.

[49] G. Kresse, J. Furthmüller, *Comput. Mater. Sci.* **1996**, *6*, 15.

[50] J. P. Perdew, K. Burke, M. Ernzerhof, *Phys. Rev. Lett.* **1996**, *77*, 3865.

[51] H. J. Monkhorst, J. D. Pack, *Phys. Rev. B* **1976**, *13*, 5188.

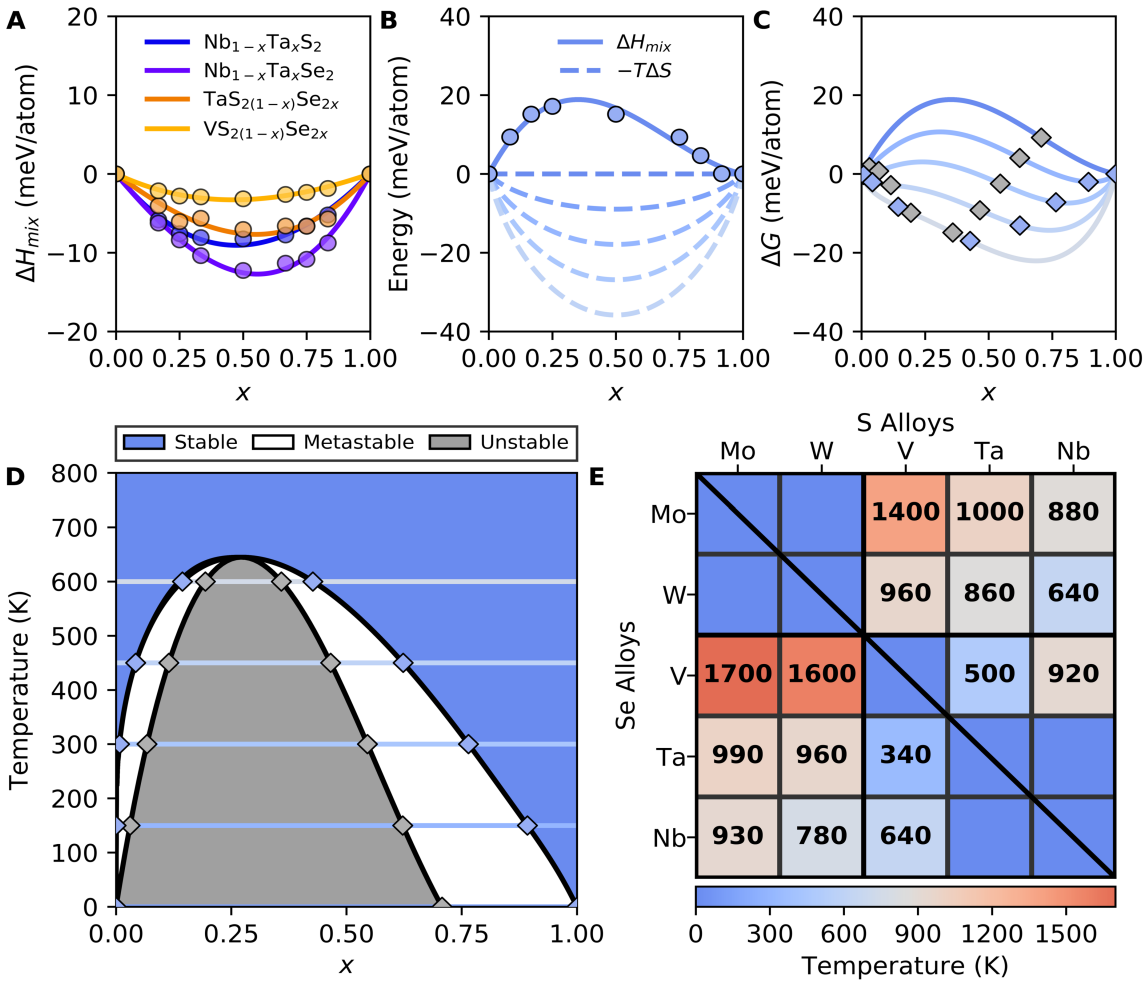

Figure 1. Theoretical predictions of the stability of the TM-site TMDC alloys. (A) Negative mixing enthalpies of $Nb_{1-x}Ta_xS_2$, $Nb_{1-x}Ta_xSe_2$, $VS_{2(1-x)}Se_{2x}$, and $TaS_{2(1-x)}Se_{2x}$, the newly predicted miscible alloys. **(B)** DFT calculated and fitted mixing enthalpy of $W_{1-x}Nb_xS_2$, along with the entropy contribution to the free energy at temperatures between 0 and 600 K in 150 K increments. **(C)** The x-dependent free energy of $W_{1-x}Nb_xS_2$ found by adding the enthalpy and entropy terms from **(B)**. The blue and grey diamonds correspond to boundary points between different stability regions in the equilibrium phase diagram. **(D)** The horizontal lines correspond one-to-one in color and temperature with the free energies in **(C)**. **(E)** The miscibility temperatures of all the 20 TM-site TMDC alloys. The top right and bottom left triangles correspond to sulfide and selenide alloys respectively while the diagonal corresponds to chalcogen-site alloys. Dark blue spaces correspond to miscible alloys.

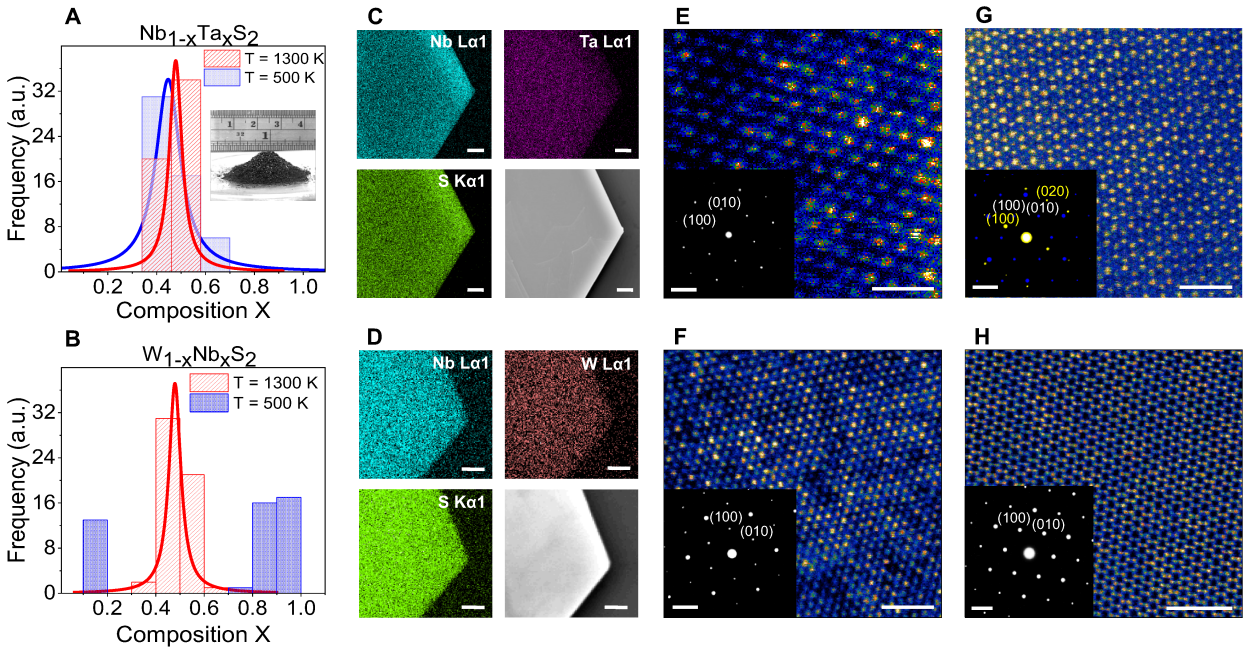

Figure 2. Summary of characterization of $Nb_{1-x}Ta_xS_2$, $W_{1-x}Nb_xS_2$, $Mo_{1-x}V_xS_2$, and $MoS_{2(1-x)}Se_{2x}$ samples selected from 12 synthesized alloys . (A, B) EDX frequency distribution of $Nb_{1-x}Ta_xS_2$ and $W_{1-x}Nb_xS_2$ samples grown at the temperature of 500 K (blue) and 1300 K (red). Inset shows the powder collected from the quartz ampoules. **(C, D)** EDX elemental maps obtained from the $Nb_{1-x}Ta_xS_2$ and $W_{1-x}Nb_xS_2$ flakes (scale bar: 1 μm). **(E, F)** Representative atomic-resolution HAADF image of [001] $Nb_{1-x}Ta_xS_2$ and $W_{1-x}Nb_xS_2$ (scale bar: 1 nm) which shows that the transition metal sites are occupied by both elements, and no sign of phase separation is found. Inset contains a SAED pattern labeled according to the 2H phase (scale bar: 2 nm^{-1}). **(G, H)** Atomic-resolution HAADF image of $Mo_{1-x}V_xS_2$ (scale bar: 1 nm) and $MoS_{2(1-x)}Se_{2x}$ (scale bar: 2 nm) in the [001] orientation. Inset shows a SAED pattern (scale bar: 2 nm^{-1}), indexed according to the 2H phase. While $Mo_{1-x}V_xS_2$ phase-separated into MoS_2 (shown in G) and VS_2 (shown in diffraction pattern only), $MoS_{2(1-x)}Se_{2x}$ appears to be alloyed as expected.

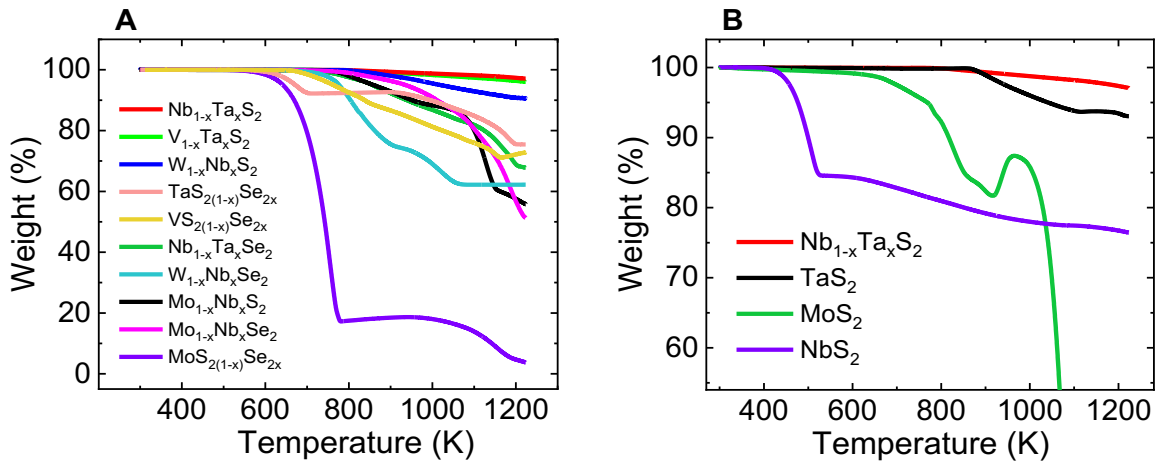

Figure 3. Thermal gravimetric analysis (TGA) curves for **(A)** As-synthesized alloys and **(B)** Unary alloys of $Nb_{1-x}Ta_xS_2$ and MoS_2 for structural integrity comparison.

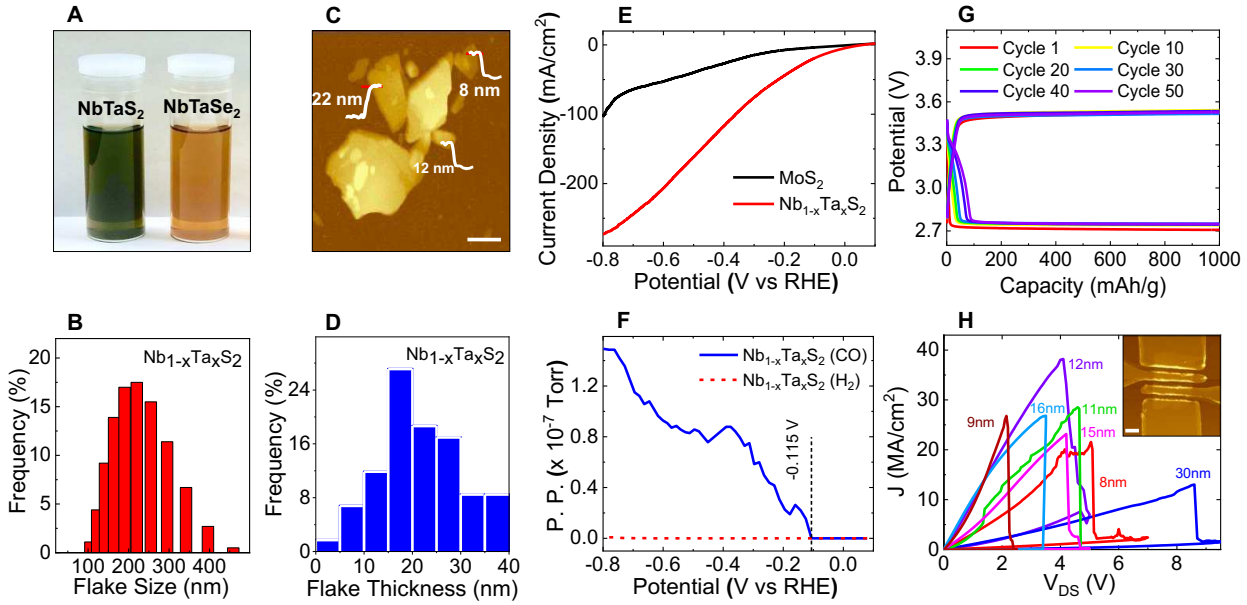

Figure 4. Electrochemical CO_2 reduction, Li-air battery and electrical performance of the $Nb_{1-x}Ta_xS_2$ alloys. **(A)** Dispersions of exfoliated nanoflakes of $Nb_{1-x}Ta_xS_2$ and $Nb_{1-x}Ta_xSe_2$ in IPA solvent. **(B)** Size distribution of synthesized $Nb_{1-x}Ta_xS_2$ alloy obtained by DLS measurements. **(C)** Typical AFM topography image of individual liquid-exfoliated flakes with the heights of 8 and 22 nm (Scale bar is 200 nm). **(D)** Frequency distribution of flake thickness obtained by AFM measurements on ~50 randomly selected exfoliated flakes. **(E)** LSV results for electrochemical reduction of CO_2 in 1 M choline chloride and 1 M potassium hydroxide using $Nb_{1-x}Ta_xS_2$ (red) and MoS_2 (black) at a scan rate of 1 $mV.s^{-1}$. **(F)** DEMS results for CO (blue) and H_2 (red dotted) production during the LSV experiment using $Nb_{1-x}Ta_xS_2$**.** CO_2 partial pressure starts to increase at 0.115V. **(G)** Discharge-charge voltage profiles for 50 cycles operation of Li-air battery. **(H)** Measured current density versus voltage characteristics of $Nb_{1-x}Ta_xS_2$ devices at 300 K approaching high breakdown current density of 40 $MA.cm^{-2}$. Inset shows the AFM micrograph of a four-probe tested structure (Scale bar is 2 µm).

Supporting Information

Quasi-Binary Transition Metal Dichalcogenide Alloys: Thermodynamic Stability Prediction, Scalable Synthesis and Application

Z. Hemmat[1§], J. Cavin[2§], A. Ahmadiparidari[1], A. Ruckel[3], S. Rastegar[1], S. N. Misal[1], L. Majidi[1], K. Kumar[4], S. Wang[3], J. Guo[3], R. Dawood[3], F. Lagunas[3], P. Parajuli[3], A. T. Ngo[5], L. A. Curtiss[5], S. B. Cho[6], J. Cabana[4], R. F. Klie[3], R. Mishra[5, 7,*], A. Salehi-Khojin[1,*]

[§]These authors contributed equally to this work.

*Corresponding authors. Email: salehikh@uic.edu (A.S.-K); rmishra@wustl.edu (R.M.)

Supporting Information

Table of Contents:

S1. Alloy phase diagrams from first-principles

Mixing Enthalpy

The enthalpy of mixing or mixing enthalpy (ΔH_{mix}) for a general quasi-binary alloy, $AB_{1-x}C_x$, is given by:

$$\Delta H_{mix}(x) = E(x) - (1-x)E_{AB} - xE_{AC}. \quad (1)$$

Here x is the molar concentration of C, $E(x)$ is the concentration-dependent DFT total energy of the alloy and E_{AB} and E_{AC} are the energies of the end-members AB and AC. In the case of the quasi-binary TMDC alloys, B and C are transition metals for TM-site alloys and are chalcogens for chalcogen-site alloys, respectively. We calculate the enthalpy by using DFT energies for SQS's corresponding to alloys of desired molar concentration and the corresponding pure TMDCs. Example plots of mixing enthalpy are shown in Figure 1A, B and all mixing enthalpies are shown in Figure S1.

A typical strategy for getting an analytical fit for the mixing enthalpy involves using the regular solution model, which corresponds to a single-parameter parabolic fit.

$$\Delta H_{\mathrm{mix}} = \Omega x(1-x). \quad (2)$$

In this expression, Ω represents the difference in the bond energies (U) between like and unlike atomic species $\Omega = 2U_{MM'} - U_M - U_{M'}$. In the case of the quasi-binary TMDC alloys though, several of the mixing enthalpies are asymmetric with respect to molar concentration. An example is shown in Figure 1B, which plots the mixing enthalpy of $W_{1-x}Nb_xS_2$. We, therefore, employ a subregular solution model, which uses a cubic fit and can be thought of an average of two regular solution models weighted by two interaction coefficients Ω_1 and Ω_2:

$$\Delta H_{\text{mix}} = [\Omega_1 x + \Omega_2(1-x)]x(1-x). \quad (3)$$

We also fit the mixing enthalpies of the stable alloys with a subregular solution model to guide the eye. In this case, we used a 4th order subregular solution model to account for the diminished curvature of the mixing enthalpy of miscible alloys. Such a fit has the form

$$\Delta H_{\text{mix}} = [\Omega_1 + \Omega_2 x + \Omega_3 x^2]x(1-x). \quad (4)$$

Entropy

The entropy ΔS in the expression $\Delta G = \Delta H_{mix} - T\Delta S$ corresponds to an entropy difference between the alloy and its end-members:

$$\Delta S(x) = S(x) - (1-x)S(0) - xS(1). \quad (5)$$

Here we only consider the increase in configurational entropy on alloying the pure TMDCs and ignore the change in vibrational entropy upon alloying in the interest of high-throughput screening. The configurational entropy is defined as the logarithm of the multiplicity of occupation configurations:

$$\Delta S(x) = k_B \ln \Omega_x \quad (6)$$

In a fully disordered alloy with N formula units, g alloyed sites per formula unit, and molar concentration x, the multiplicity is given by:

$$\Omega_x = \frac{gN!}{(xgN)!\,([1-x]gN)!} = \frac{\Gamma(gN+1)}{\Gamma(xgN+1)\Gamma([1-x]gN+1)}. \quad (7)$$

For large N, the Sterling approximation gives:

$$\Omega_x = \frac{1}{\sqrt{2\pi x(1-x)}}(x^x(1-x)^{1-x})^{-gN}. \quad (8)$$

Taking the logarithm, dividing by N, and discarding the negligible term gives the configurational entropy per formula unit:

$$\Delta S = -gk_B[x\ln(x) + (1-x)\ln(1-x)]. \quad (9)$$

In the case of TM-site alloys $g = 1$, whereas chalcogen-site alloys have $g = 2$.

Equilibrium Phase Diagram

Developing an equilibrium phase diagram for an alloy requires analyzing the molar concentration-dependent free energy for a grid of temperature values. The free energy with respect to the endpoints of an alloy is given by:

$$\Delta G_{mix}(x;T) = \Delta H_{mix}(x) - T\Delta S(x). \quad (2)$$

At each temperature value, the molar concentration is divided into three regions: a stable region, a metastable region, and an unstable region. In the stable region, a corresponding disordered alloy has lower free energy than any phase segregation. This is shown in the two regions outside each pair of blue diamonds in Figure 1C. In between the pairs of blue diamonds, the free energy of a disordered alloy is higher than that of a partial decomposition into phases with molar concentrations corresponding to the blue diamond pairs. These pairs of blue diamonds are determined by the common tangent method and correspond to the boundary between the stable and metastable regions known as the binodal boundary. Figure 1D shows the binodal boundary of $W_{1-x}Nb_xS_2$ with the same blue diamonds corresponding to the temperatures in Figure 1C.

Within the blue diamonds, the alloy is either metastable or unstable. The grey diamonds in Figure 1C correspond to inflection points and within them, the second derivative of the free energy with

respect to molar concentration is negative, i.e. $\frac{\mathrm{d}^2}{\mathrm{d}x^2}\Delta G_{mix} < 0$. In this region, any fluctuation in local molar concentration is energetically stable and therefore leads to phase segregation. For this reason, this region is an unstable region. Between the blue and grey diamond pairs, however, the second derivative of the free energy is positive and so this region is rigid to phase decomposition by local fluctuations in molar concentration. This region is still not the thermodynamically most stable region, because decomposing into the two blue diamond points is more stable by the common tangent law. Because the alloy is stable to these local fluctuations but is not the global ground state, this is the metastable region. These pairs of grey diamonds, therefore, correspond to the boundary between the metastable and unstable regions known as the spinodal boundary. Figure 1D shows the spinodal boundary of $W_{1-x}Nb_xS_2$ with the same grey diamonds corresponding to the temperatures in Figure 1C. Figures S1-S3 show the mixing enthalpies for all 25 quasi-binary TMDC alloys separated into miscible alloys and immiscible sulfide and selenide alloys. For the immiscible alloys, equilibrium phase diagrams are shown in Figure S4 and S5. Figure S6 shows that the alloys obey Vegard's law with plots of lattice parameters as a function of composition. Table S1 is a comprehensive list of all 25 alloys studied arranged in the same manner as Figure 1E. Table S2 shows the energy per formula unit of the *1T* and *1T'* phases with respect to the *2H* phase, confirming the stability of the *2H* phase for all 10 end-member TMDCs.

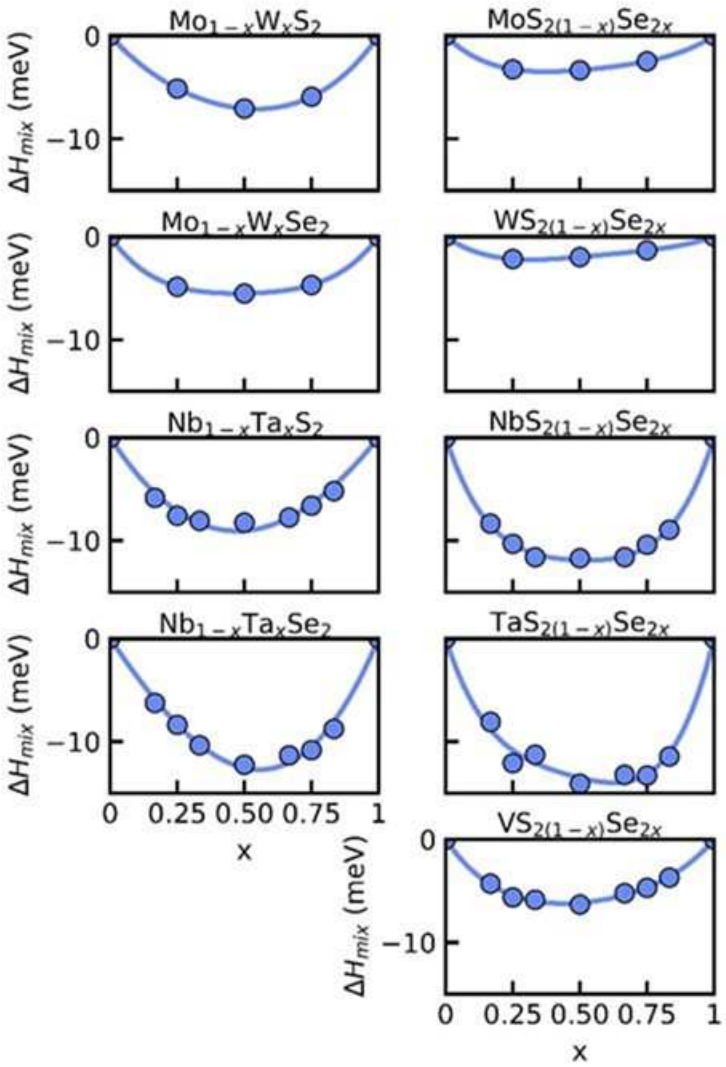

Figure S1. DFT mixing enthalpies of the 9 miscible quasibinary TMDC alloys. The left column has the TM-site alloys and the right column has chalcogen-site alloys. The top four are group VI TMDC alloys and the bottom five are group V TMDC alloys. Enthalpies are given in meV per formula unit.

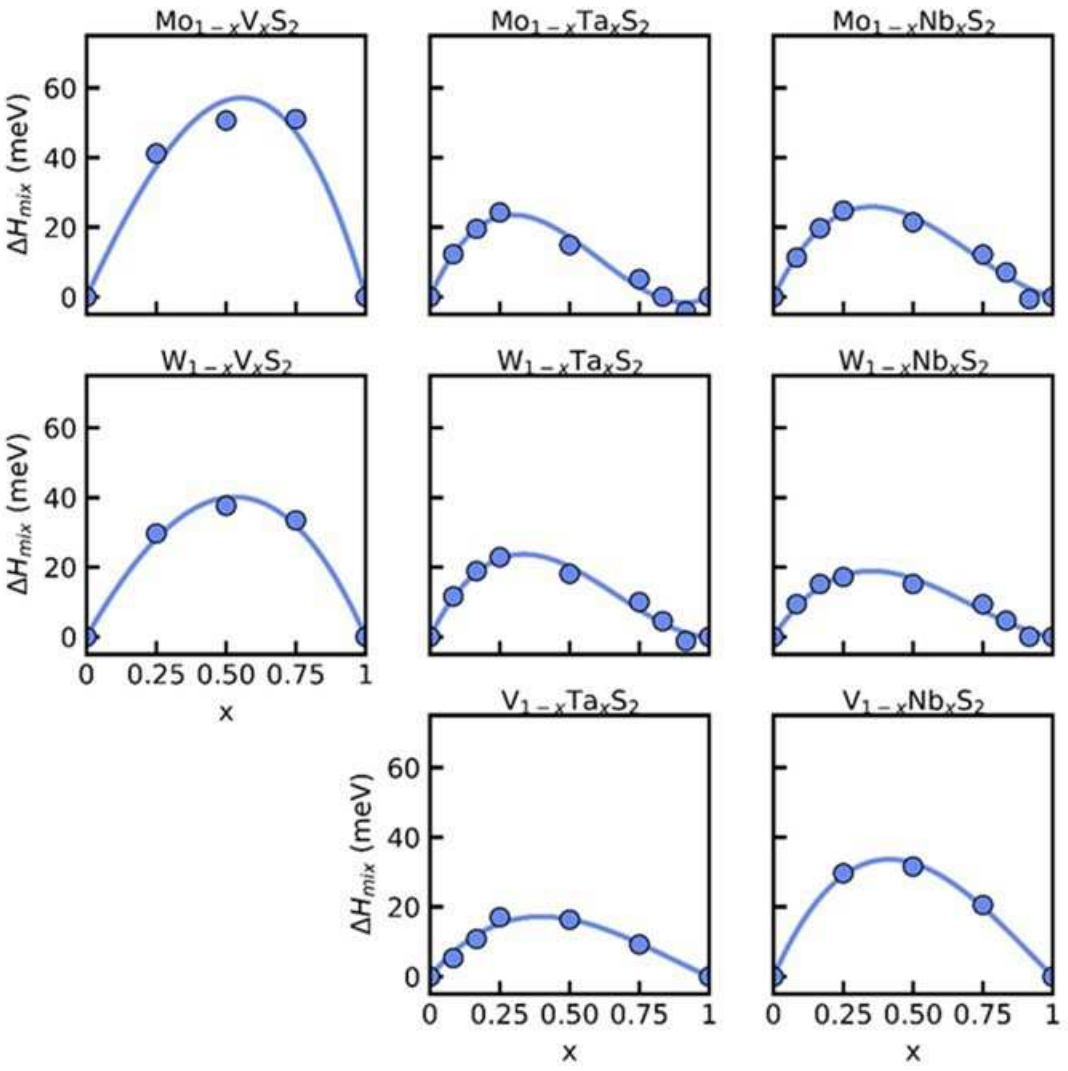

Figure S2. DFT mixing enthalpies for immiscible sulfide quasibinary TMDC alloys. Enthalpies are given in meV per formula unit.

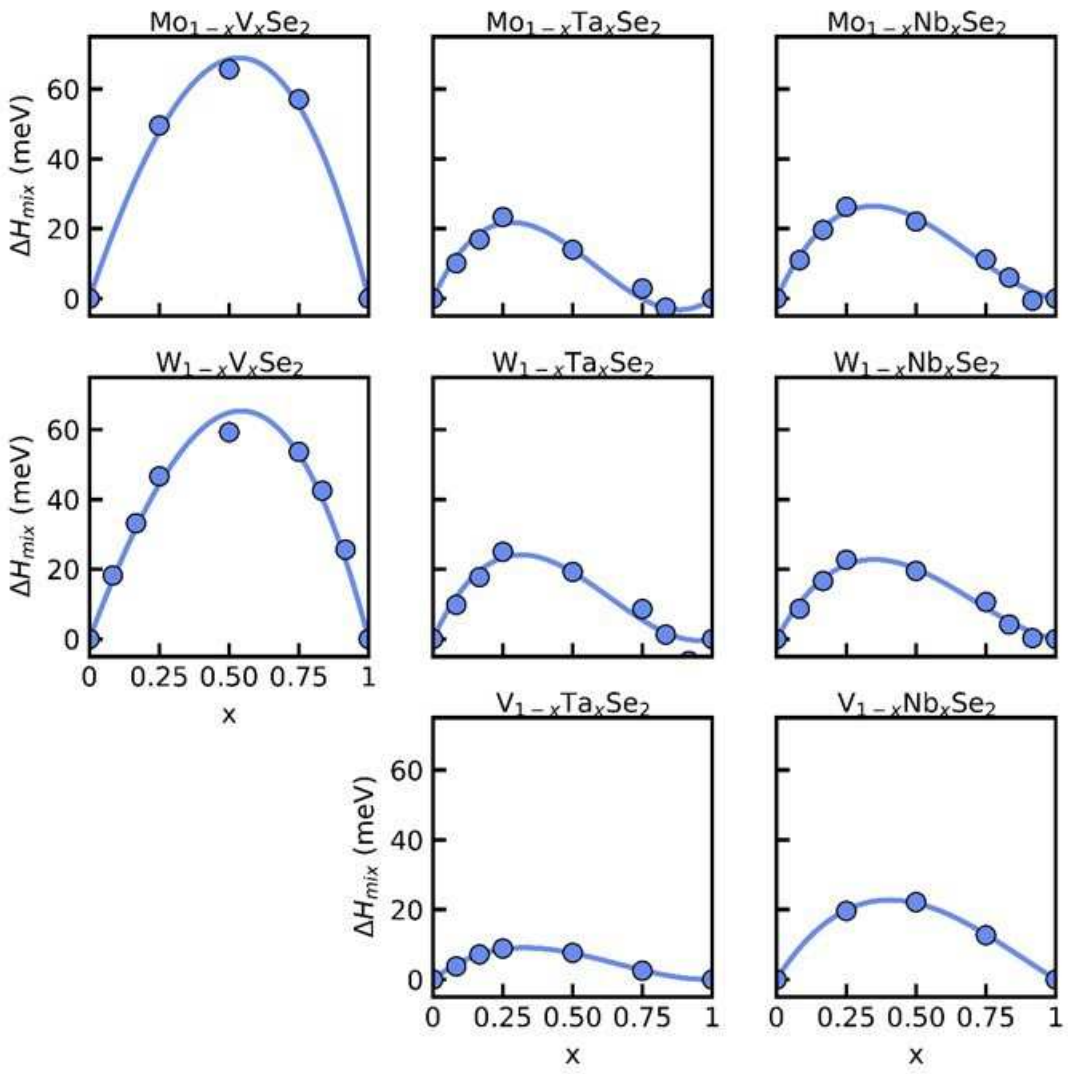

Figure S3. DFT mixing enthalpies for immiscible selenide quasibinary TMDC alloys. Enthalpies are given in meV per formula unit.

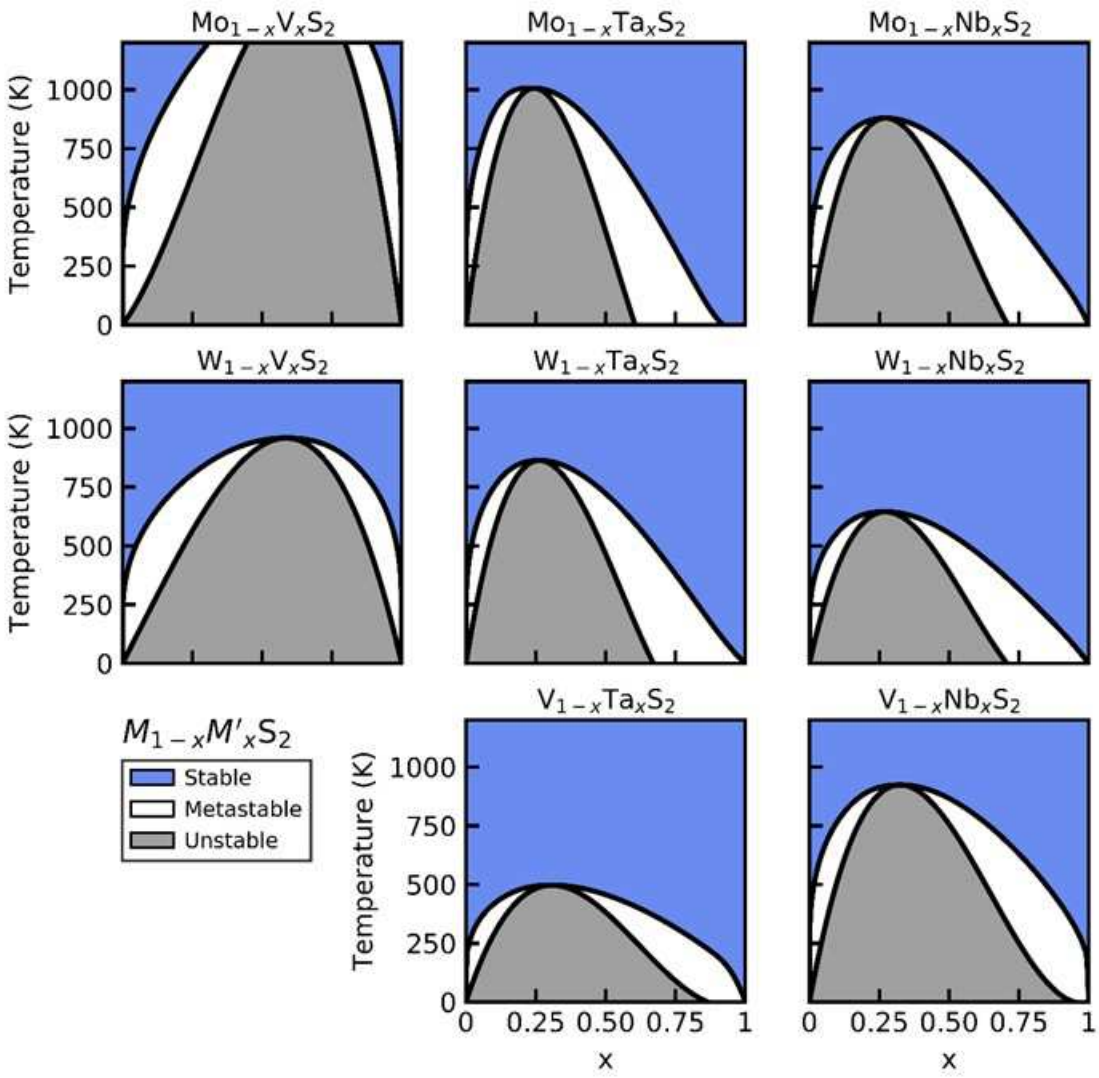

Figure S4. Equilibrium phase diagrams for all 8 immiscible sulfide TMDC alloys.

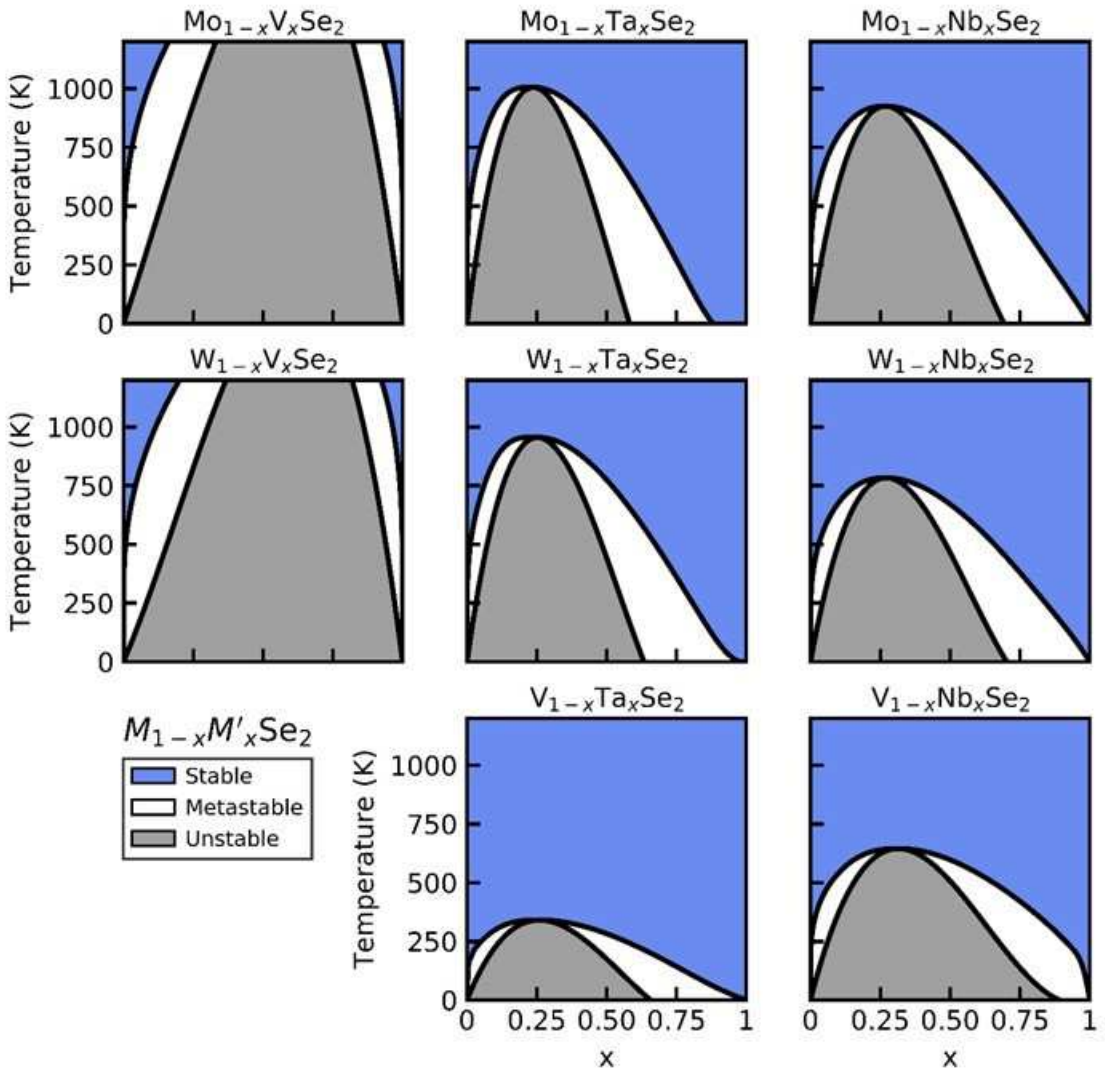

Figure S5. Equilibrium phase diagrams for all 8 immiscible selenide TMDC alloys.

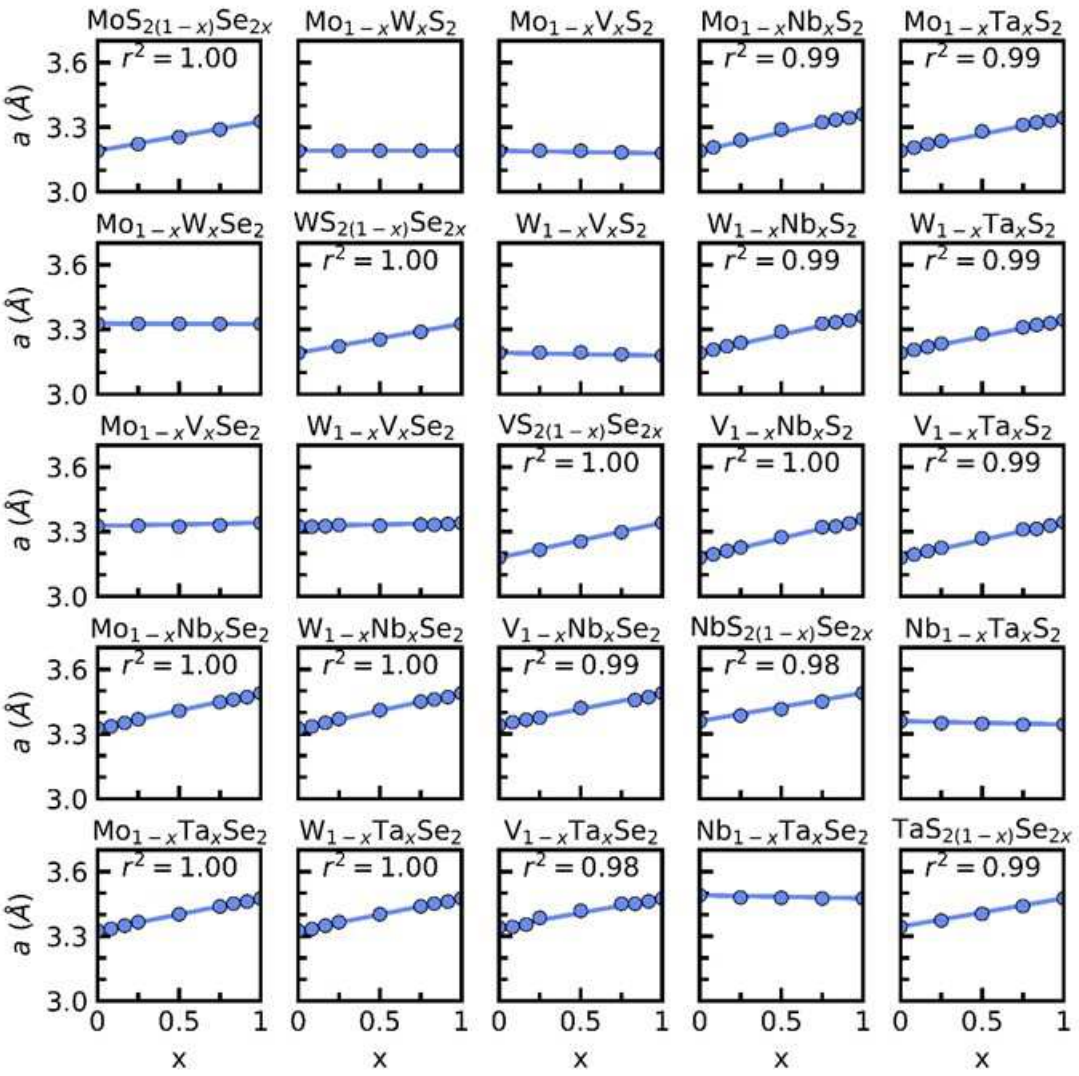

Figure S6. Lattice vector as a function of molar concentration for all 25 TMDC alloys. The straight lines correspond to the Vegard's law lattice parameter with r^2 showing the goodness of the fit.

Table S1: List of all 25 TMDC alloys studied.

	Mo	W	V	Nb	Ta
Mo	$MoS_{2(1-x)}Se_{2x}$	$Mo_{1-x}W_xS_2$	$Mo_{1-x}V_xS_2$	$Mo_{1-x}Nb_xS_2$	$Mo_{1-x}Ta_xS_2$
W	$Mo_{1-x}W_xSe_2$	$WS_{2(1-x)}Se_{2x}$	$W_{1-x}V_xS_2$	$W_{1-x}Nb_xS_2$	$W_{1-x}Ta_xS_2$
V	$Mo_{1-x}V_xSe_2$	$W_{1-x}V_xSe_2$	$VS_{2(1-x)}Se_{2x}$	$V_{1-x}Nb_xS_2$	$V_{1-x}Ta_xS_2$
Nb	$Mo_{1-x}Nb_xSe_2$	$W_{1-x}Nb_xSe_2$	$V_{1-x}Nb_xSe_2$	$NbS_{2(1-x)}Se_{2x}$	$Nb_{1-x}Ta_xS_2$
Ta	$Mo_{1-x}Ta_xSe_2$	$W_{1-x}Ta_xSe_2$	$V_{1-x}Ta_xSe_2$	$Nb_{1-x}Ta_xSe_2$	$TaS_{2(1-x)}Se_{2x}$

Table S2: Relative energies of the metastable octahedral 1T and distorted octahedral 1T' phases with respect to the stable hexagonal 2H phase for all 10 pure endmember TMDCs. For group V TMDCs, the 1T' phase relaxed into the 1T phase.

	$E_{1T} - E_{2H}$ (mev/f.u.)	$E_{1T'} - E_{2H}$(meV/f.u.)
MoS_2	**838**	**549**
$MoSe_2$	**706**	**332**
WS_2	**889**	**542**
WSe_2	**774**	**279**
VS_2	**43**	**43**
VSe_2	**42**	**42**
NbS_2	**104**	**106**
$NbSe_2$	**98**	**99**
TaS_2	**64**	**66**
$TaSe_2$	**70**	**72**

S2. Transmission electron microscopy (TEM) measurement

Figures S7-S9 show the TEM and STEM micrographs for $Nb_{1-x}Ta_xS_2$, $Nb_{1-x}Ta_xS_2$, and $W_{1-x}Nb_xS_2$. All the images are shown in the (001) orientation, displaying a hexagonal symmetry. The corresponding electron diffraction patterns are shown in Figures S7C-S9C. Analysis of the TEM/STEM images, the electron diffraction patterns as well as image simulations confirms that all three samples are 2H phase, and we did not detect any sign of phase separation in the samples.

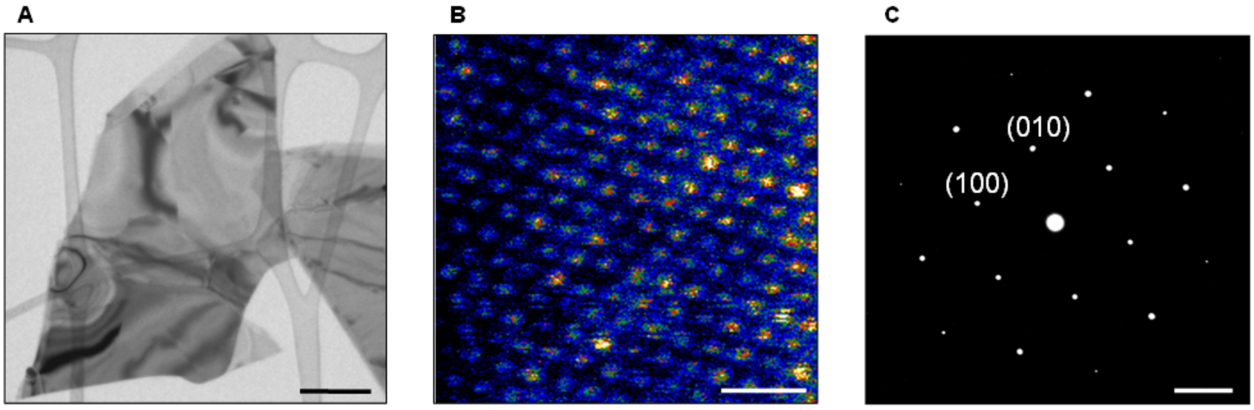

Figure S7. $Nb_{1-x}Ta_xS_2$ sample. (A) Low magnification TEM image of a thin particle (scale bar: 500nm), **(B)** atomic-resolution STEM image (scale bar: 1nm) and **(C)** electron diffraction pattern of the flake show in **(A)** (scale bar: $2nm^{-1}$). The atomic-resolution image and diffraction pattern match the 2H phase showing no sign of phase separation.

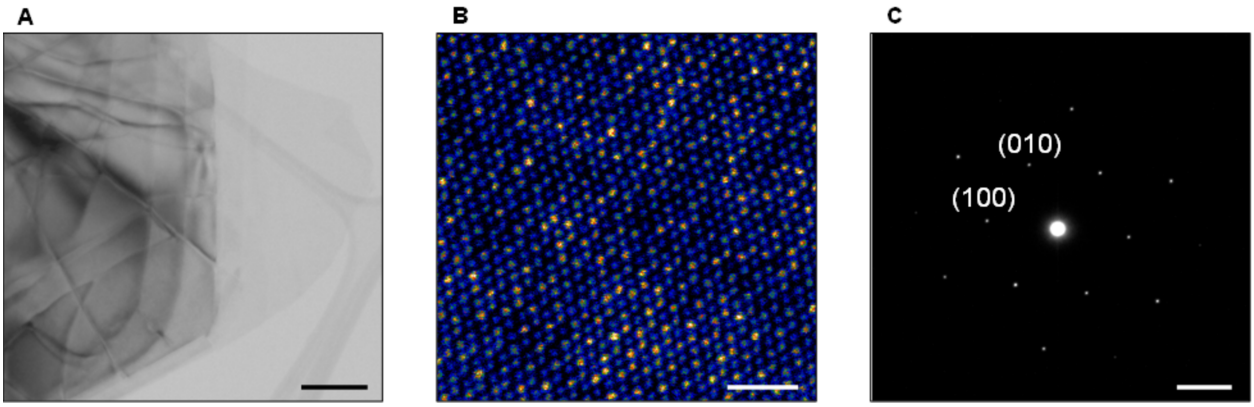

Figure S8. $Nb_{1-x}Ta_xSe_2$ sample. (A) Low magnification TEM image of a thin particle (scale bar: 200nm), **(B)** atomic-resolution STEM image (scale bar: 1nm) and **(C)** electron diffraction pattern of the flake show in **(A)** (scale bar: $2nm^{-1}$). The atomic-resolution image and diffraction pattern match the 2H phase showing no sign of phase separation.

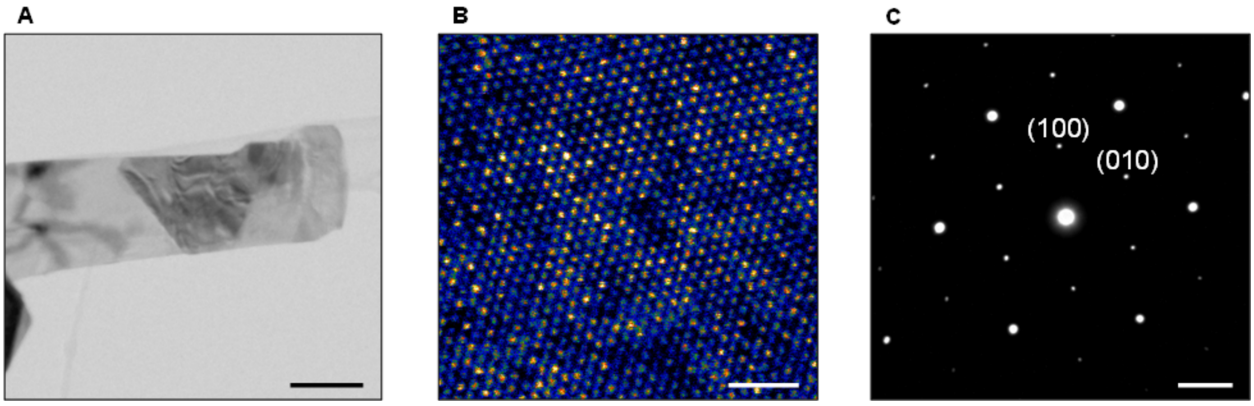

Figure S9. $W_{1-x}Nb_xS_2$ sample. **(A)** Low magnification TEM image of a thin particle (scale bar: 200nm), **(B)** atomic-resolution STEM image (scale bar: 1nm) and **(C)** electron diffraction pattern of the flake show in **(A)** (scale bar: $2nm^{-1}$)**.** The atomic-resolution image and diffraction pattern match the 2H phase showing no sign of phase separation.

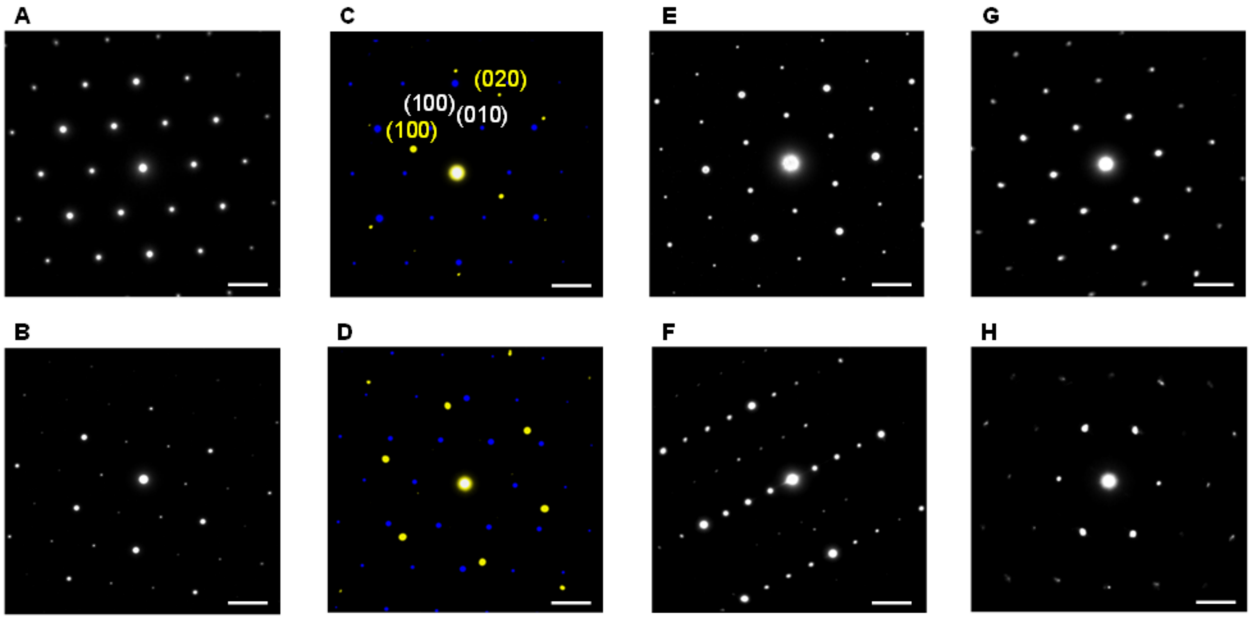

Figure S10. Electron diffraction patterns. **(A)** 2H $Mo_{1-x}Nb_xS_2$, **(B)** 2H $Mo_{1-x}Nb_xSe_2$, **(C)** $Mo_{1-x}V_xS_2$, showing phase separation into MoS_2 and VS_2 (shown in yellow and blue), **(D)** phase separated $Mo_{1-x}V_xSe_2$ with the two diffraction patterns for $MoSe_2$ and VSe_2 are overlaid in blue and yellow; **(E)** 2H $TaS_{2(1-x)}Se_{2x}$; **(F)** $VS_{2(1-x)}Se_{2x}$; **(G)** 2H $V_{1-x}Ta_xS_2$ and **(H)** $W_{1-x}Nb_xSe_2$ (scale bars: $2nm^{-1}$).

Table S3: In-plane lattice parameters *(a, b, γ)* as measured from SAEDP orthogonal to the [001] zone axis. EDS-TEM spectra determined the atomic composition for phase segregated $Mo_{1-x}V_xSe_2$ and $Mo_{1-x}V_xS_2$. The magnitude of the $\boldsymbol{a}_2$ basis vector for $Mo_{0.05}V_{0.95}S_2$ was approximated from the (020) diffraction spot. Measured parameters for $VS_{2(1-x)}Se_{2x}$ correspond to triclinic VS_2 with 6.88% Se concentration.

Alloy	*a* [Å]	*b* [Å]	*γ*[°]
$V_{1-x}Ta_xS_2$	**3.36**	**3.03**	**116.2**
$Nb_{1-x}Ta_xS_2$	**3.23**	**3.21**	**121.1**
$Nb_{1-x}Ta_xSe_2$	**3.09**	**3.11**	**118.8**
$W_{1-x}Nb_xSe_2$	**3.27**	**2.71**	**115.5**
$W_{1-x}Nb_xS_2$	**3.03**	**3.01**	**119.3**
$Mo_{1-x}Nb_xS_2$	**3.14**	**3.16**	**120.3**
$Mo_{1-x}Nb_xSe_2$	**3.32**	**3.30**	**120.4**
$Mo_{0.84}V_{0.16}Se_2$	**3.23**	**3.18**	**120.4**
$Mo_{0.02}V_{0.98}Se_2$	**3.39**	**3.42**	**120.9**
$Mo_{0.95}V_{0.05}S_2$	**3.08**	**3.03**	**121.1**
$Mo_{0.05}V_{0.95}S_2$	**2.86**	**3.65**	**89.2**
$MoS_{2(1-x)}Se_{2x}$	**3.09**	**3.07**	**120.0**
$VS_{2(1-x)}Se_{2x}$	**5.59**	**3.11**	**73.9**
$TaS_{2(1-x)}Se_{2x}$	**3.28**	**3.28**	**119.5**

S3. STEM Image Simulations

STEM HAADF image simulations were performed using the μSTEM multislice software (tcmp.ph.unimelb. edu.au/mustem) with defocus (Δf) -23.17 Å, 3rd order spherical aberration 18,440 Å, 3-Fold astigmatism 79.65 Å, 3-Fold astigmatism 2.335 Å and an inner detector angle of 90 with a maximum detector angle of 370 mrads. All samples shown here are 10 nm sample thickness. The aberration and detector parameters are chosen to match the experimental setup. Figure S11 clearly shows that all STEM images shown in Figure 2E-H match the simulated images of the 2H phase.

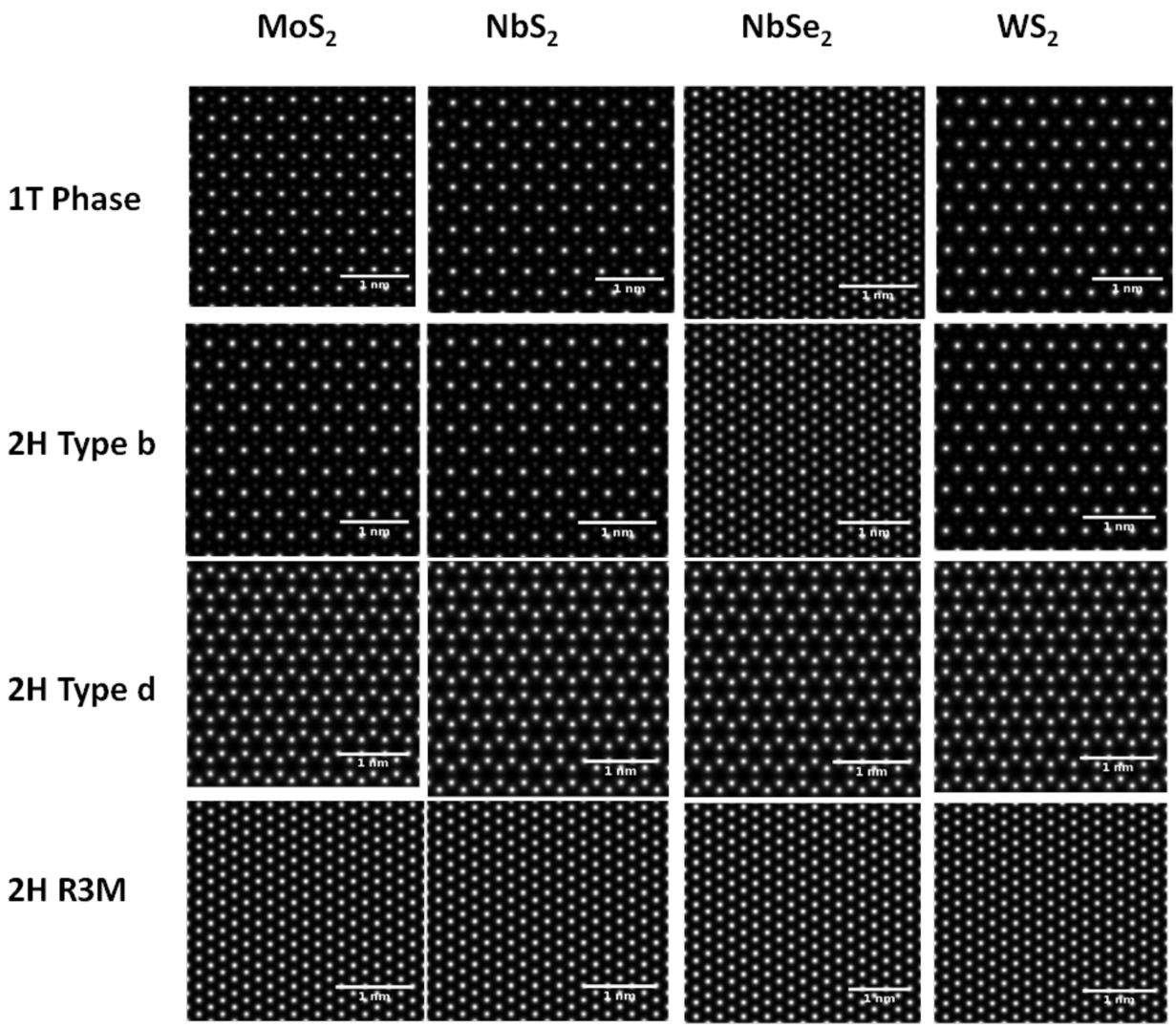

Figure S11. STEM Image Simulations: Atomic-resolution high-angle annular dark field image simulations for 4 pure TMDs in different possible phases and stackings. All images are shown in the (001) orientation.

S4. Energy Dispersive X-Ray Spectroscopy (EDX)

Figures S12-23 represent the summary of Scanning Electron Microscopy (SEM) -EDX characterization for $Nb_{1-x}Ta_xS_2$, $Nb_{1-x}Ta_xSe_2$, $W_{1-x}Nb_xS_2$, $W_{1-x}Nb_xSe_2$, $Mo_{1-x}Nb_xS_2$, $Mo_{1-x}Nb_xSe_2$, $MoS_{2(1-x)}Se_{2x}$, $VS_{2(1-x)}Se_{2x}$, $TaS_{2(1-x)}Se_{2x}$, $V_{1-x}Ta_xS_2$, $Mo_{1-x}V_xS_2$, and $Mo_{1-x}V_xSe_2$ alloys, respectively.

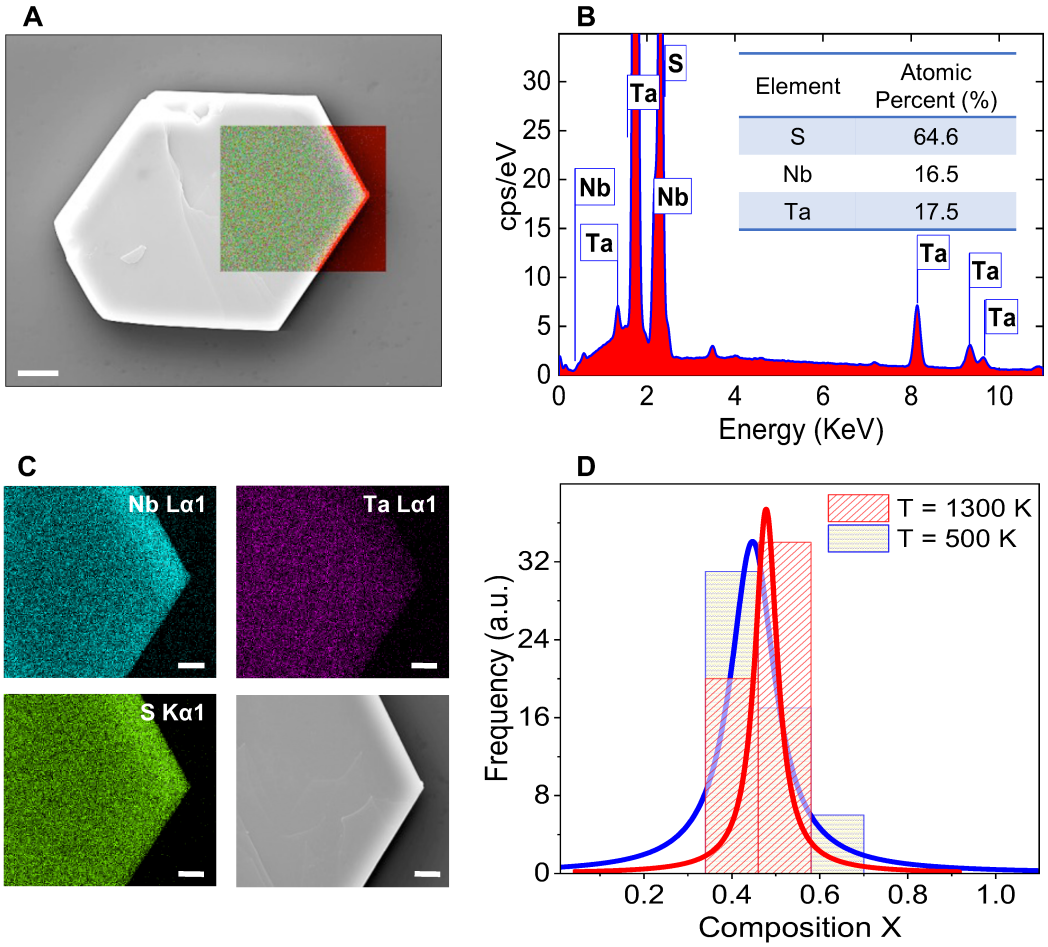

Figure S12. SEM-EDX characterization of $Nb_{1-x}Ta_xS_2$ sample. (A) SEM image of the $Nb_{1-x}Ta_xS_2$ flake (scale bar: 2μm). **(B)** EDX spectrum acquired from the area marked by a square in **(A).** The quantification results are presented in the table, showing the average stoichiometry ratio of $Nb_{0.5}Ta_{0.5}S_2$. **(C)** Full EDX composition mapping of the detected elements (scale bars: 1μm). **(D)** EDX frequency distribution from ~50-60 flakes of $Nb_{1-x}Ta_xS_2$ grown at the temperature of 1300 K (red) and 500 K (blue).

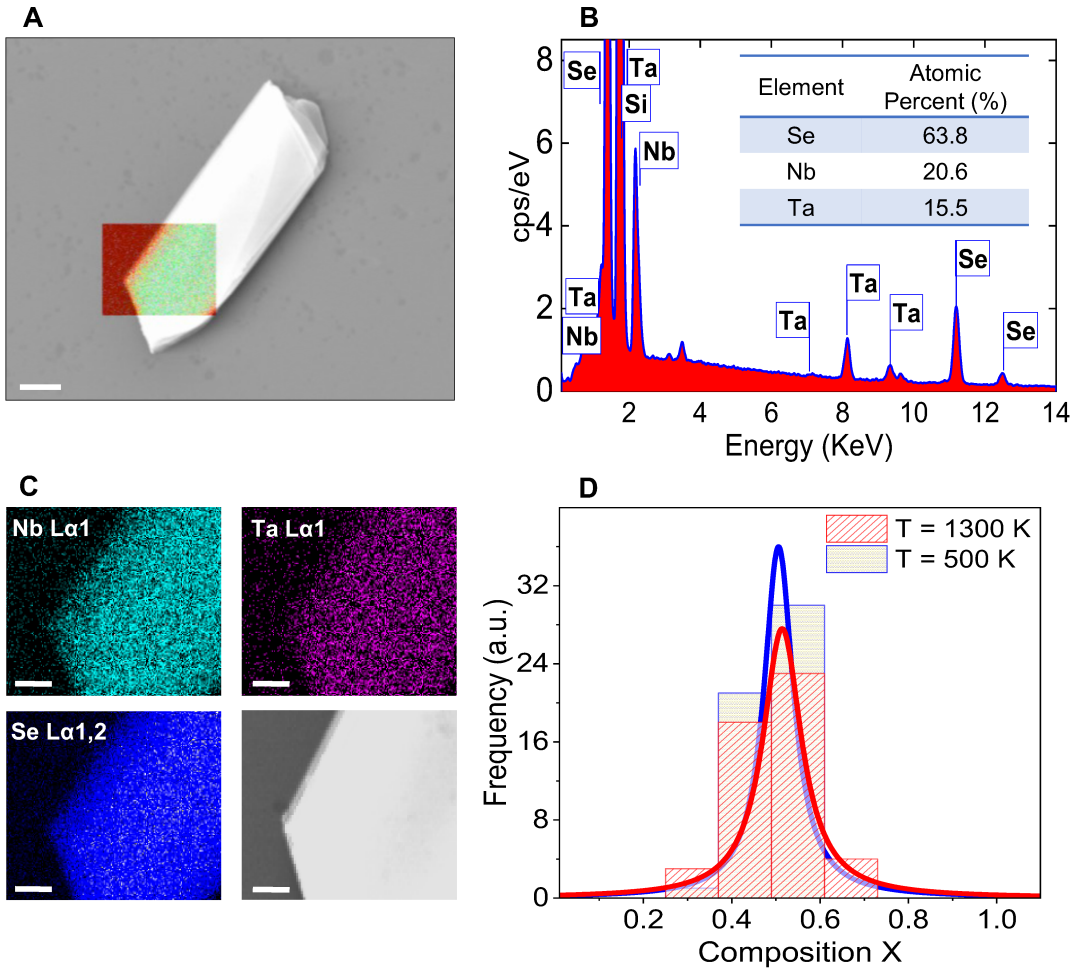

Figure S13. SEM-EDX characterization of $Nb_{1-x}Ta_xSe_2$ sample. (A) SEM image of the $Nb_{1-x}Ta_xSe_2$ flake (scale bar: 1 μm). **(B)** EDX spectrum acquired from the area marked by a square in **(A).** The quantification results are presented in the table, showing the average stoichiometry ratio of $Nb_{0.52}Ta_{0.48}Se_2$. **(C)** Full EDX composition mapping of the detected elements (scale bars: 300 nm). **(D)** EDX frequency distribution from ~50-60 flakes of $Nb_{1-x}Ta_xSe_2$ grown at the temperature of 1300 K (red) and 500 K (blue).

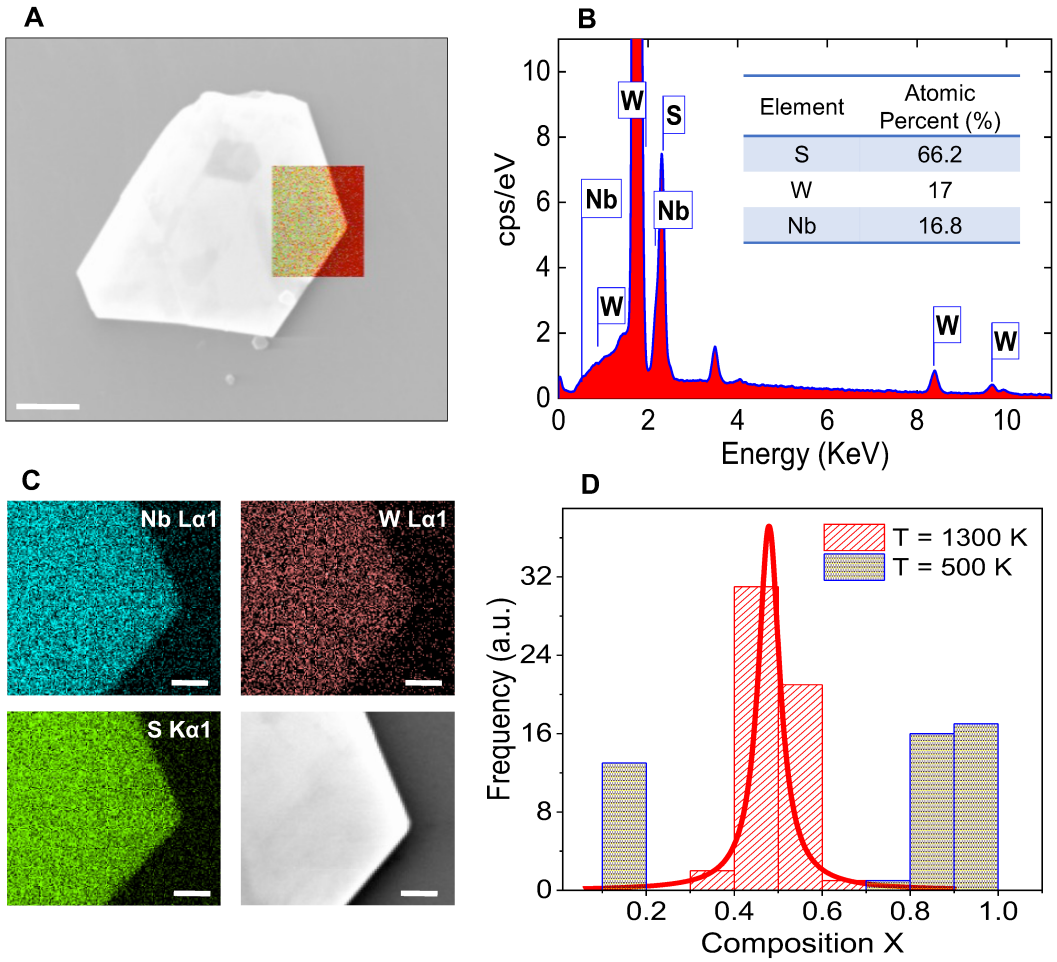

Figure S14. SEM-EDX characterization of $W_{1-x}Nb_xS_2$ sample. (A) SEM image of the $W_{1-x}Nb_xS_2$ flake (scale bar: 1 μm). **(B)** EDX spectrum acquired from the area marked by a square in **(A).** The quantification results are presented in the table, showing the average stoichiometry ratio of $W_{0.5}Nb_{0.5}S_2$. **(C)** Full EDX composition mapping of the detected elements (scale bars: 200 nm). **(D)** EDX frequency distribution from ~50-60 flakes of $W_{1-x}Nb_xS_2$ grown at the temperature of 1300 K (red) and 500 K (blue).

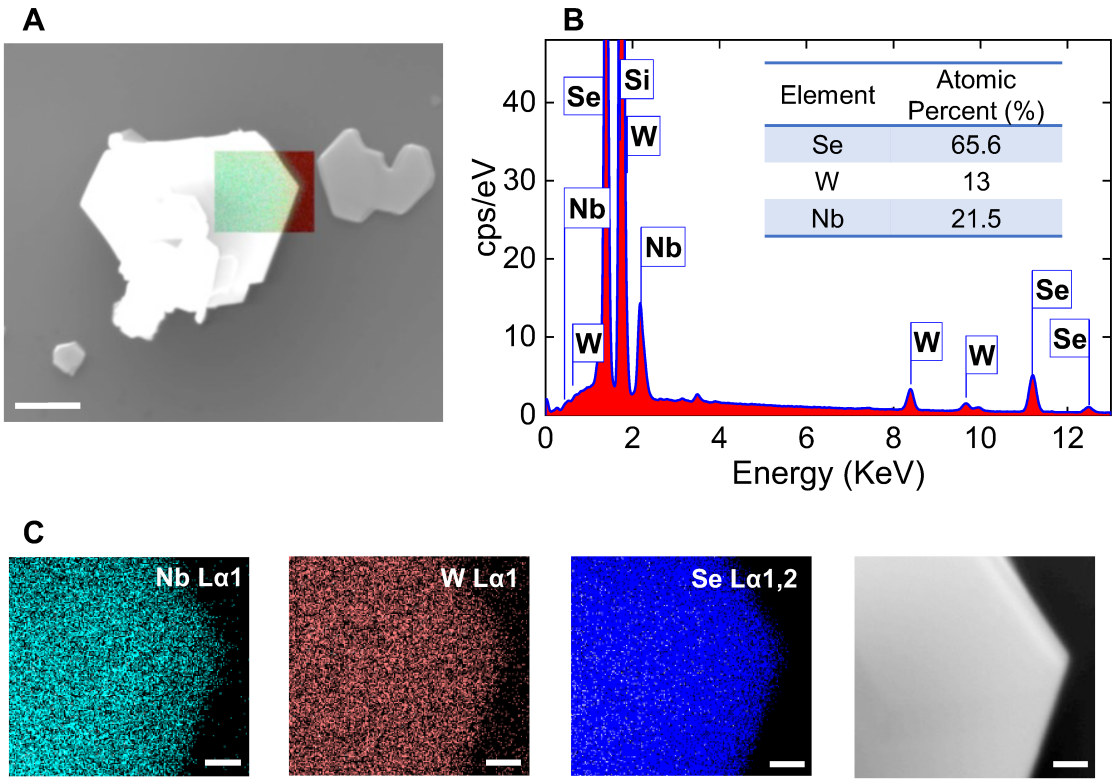

Figure S15. SEM-EDX characterization of $W_{1-x}Nb_xSe_2$ sample. (A) SEM image of the $W_{1-x}Nb_xSe_2$ flake (scale bar: 1 μm). **(B)** EDX spectrum acquired from the area marked by a square in **(A).** The quantification results are presented in the table, showing the average stoichiometry ratio of $W_{0.38}Nb_{0.62}Se_2$. **(C)** Full EDX composition mapping of the detected elements (scale bars: 200 nm).

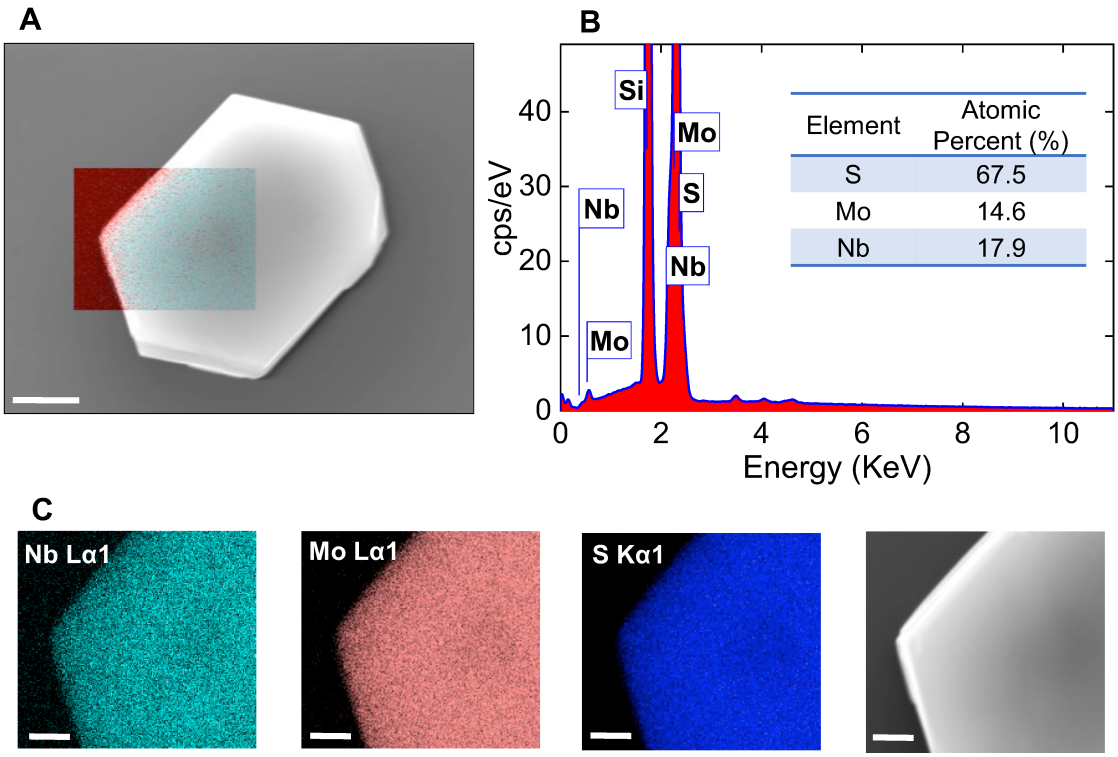

Figure S16. SEM-EDX characterization of $Mo_{1-x}Nb_xS_2$ sample. (A) SEM image of the $Mo_{1-x}Nb_xS_2$ flake (scale bar: 1 μm). **(B)** EDX spectrum acquired from the area marked by a square in **(A).** The quantification results are presented in the table, showing the average stoichiometry ratio of $Mo_{0.46}Nb_{0.53}S_2$. **(C)** Full EDX composition mapping of the detected elements (scale bars: 200 nm).

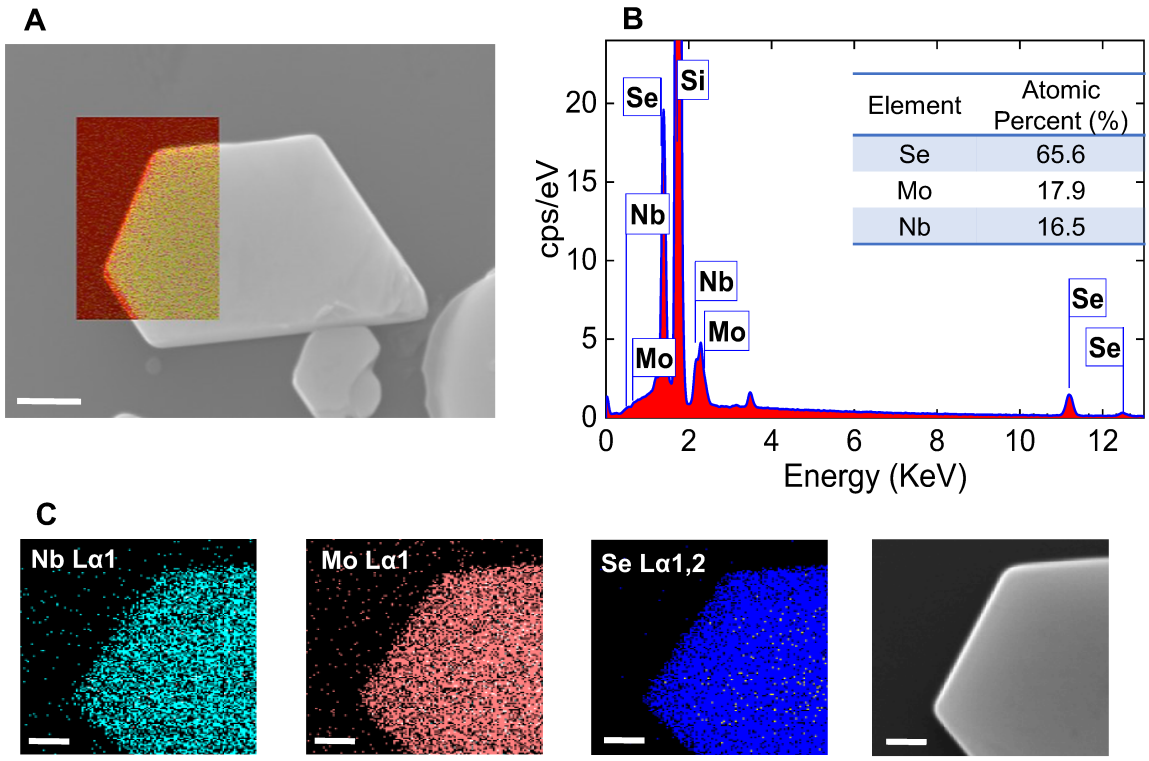

Figure S17. SEM-EDX characterization of $Mo_{1-x}Nb_xSe_2$ sample. (A) SEM image of the $Mo_{1-x}Nb_xSe_2$ flake (scale bar: 1 μm). **(B)** EDX spectrum acquired from the area marked by a square in **(A).** The quantification results are presented in the table, showing the average stoichiometry ratio of $Mo_{0.5}Nb_{0.5}Se_2$. **(C)** Full EDX composition mapping of the detected elements (scale bars: 250 nm).

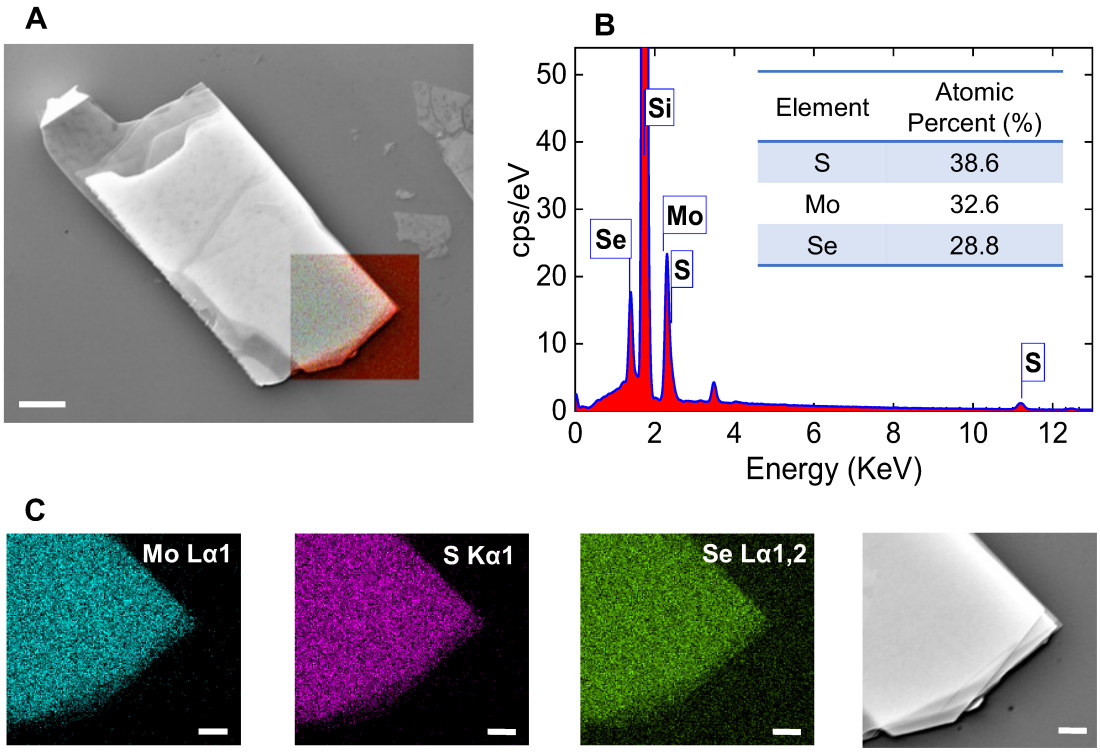

Figure S18. SEM-EDX characterization of $MoS_{2(1-x)}Se_{2x}$ sample. (A) SEM image of the $MoS_{2(1-x)}Se_{2x}$ flake (scale bar: 3 µm). **(B)** EDX spectrum acquired from the area marked by a square in **(A).** The quantification results are presented in the table, showing the average stoichiometry ratio of $MoS_{1.1}Se_{0.9}$. **(C)** Full EDX composition mapping of the detected elements (scale bars: 500 nm).

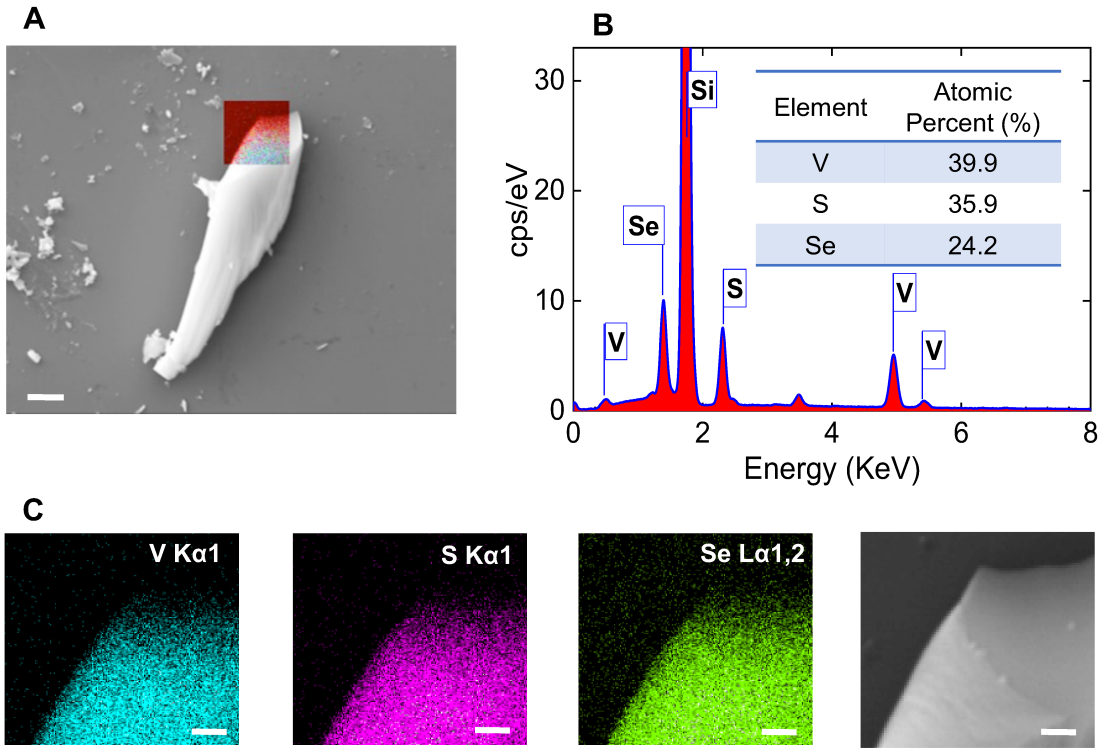

Figure S19. SEM-EDX characterization of $VS_{2(1-x)}Se_{2x}$ sample. (A) SEM image of the $VS_{2(1-x)}Se_{2x}$ flake (scale bar: 2 μm). **(B)** EDX spectrum acquired from the area marked by a square in **(A).** The quantification results are presented in the table, showing the average stoichiometry ratio of $VS_{0.89}Se_{0.6}$. **(C)** Full EDX composition mapping of the detected elements (scale bars: 500 nm).

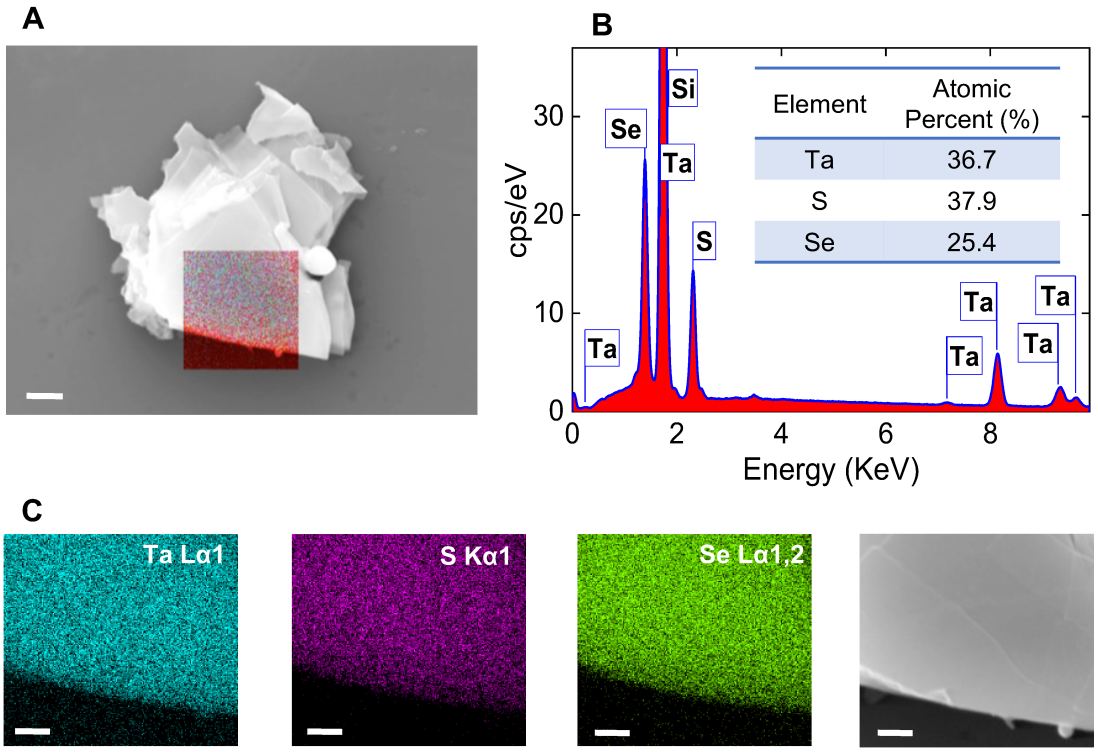

Figure S20. SEM-EDX characterization of $TaS_{2(1-x)}Se_{2x}$ sample. (A) SEM image of the $TaS_{2(1-x)}Se_{2x}$ flake (scale bar: 1 μm). **(B)** EDX spectrum acquired from the area marked by a square in **(A).** The quantification results are presented in the table, showing the average stoichiometry ratio of $TaS_{1.03}Se_{0.69}$. **(C)** Full EDX composition mapping of the detected elements (scale bars: 500 nm).

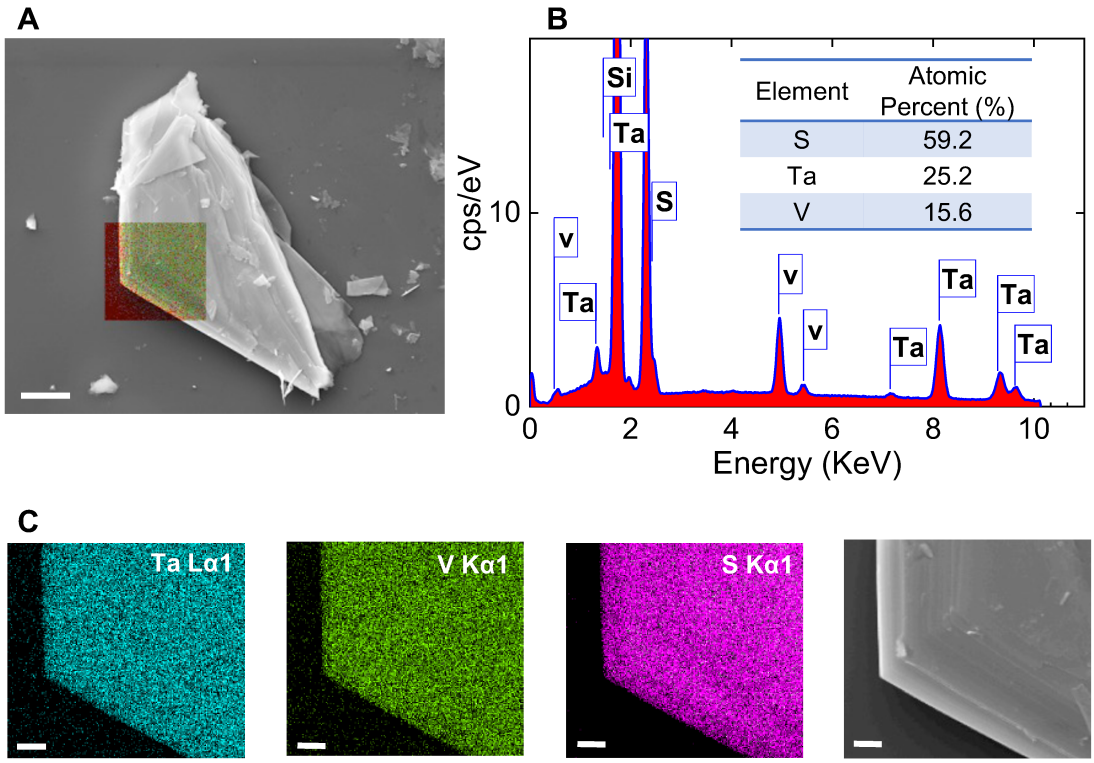

Figure S21. SEM-EDX characterization of $V_{1-x}Ta_xS_2$ sample. (A) SEM image of the $V_{1-x}Ta_xS_2$ flake (scale bar: 5 μm). **(B)** EDX spectrum acquired from the area marked by a square in **(A).** The quantification results are presented in the table, showing the average stoichiometry ratio of $V_{0.38}Ta_{0.62}S_2$. **(C)** Full EDX composition mapping of the detected elements (scale bars: 1 μm).

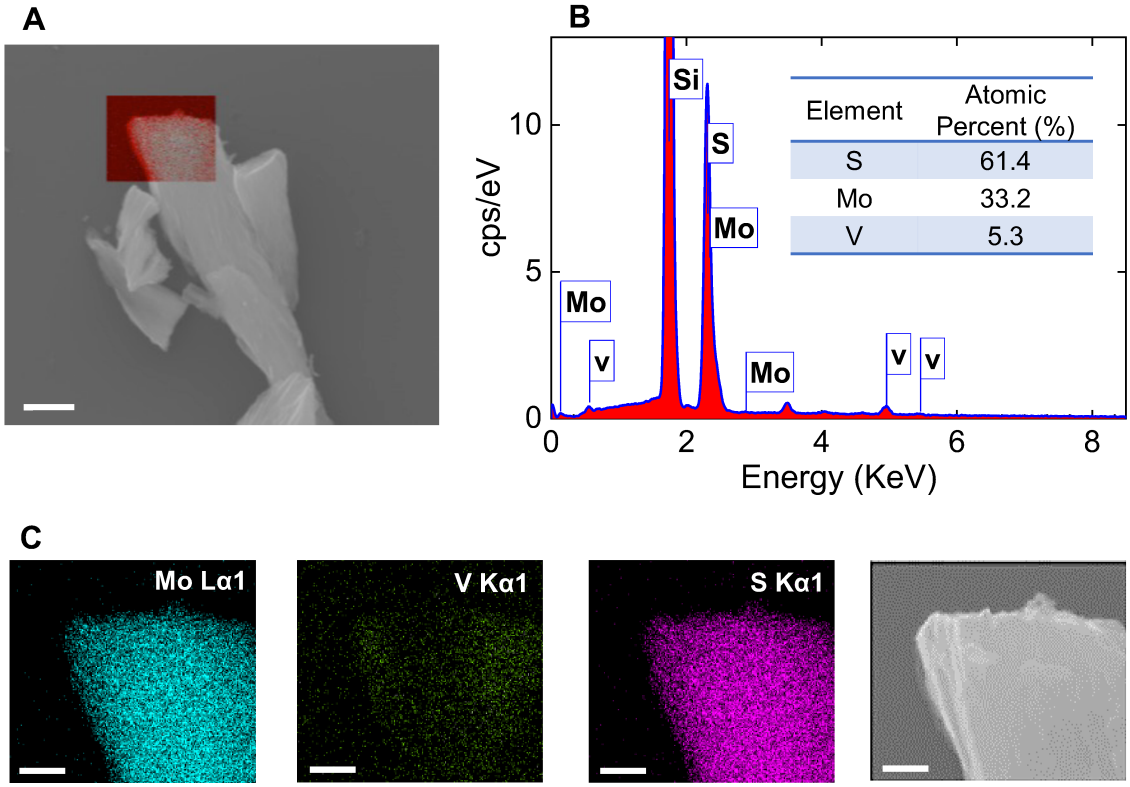

Figure S22. SEM-EDX characterization of $Mo_{1-x}V_xS_2$ sample. (A) SEM image of the $Mo_{1-x}V_xS_2$ flake (scale bar: 2 µm). **(B)** EDX spectrum acquired from the area marked by a square in **(A).** The quantification results are presented in the table, showing the average stoichiometry ratio of $Mo_{0.9}V_{0.1}S_2$. **(C)** Full EDX composition mapping of the detected elements (scale bars: 500 nm).

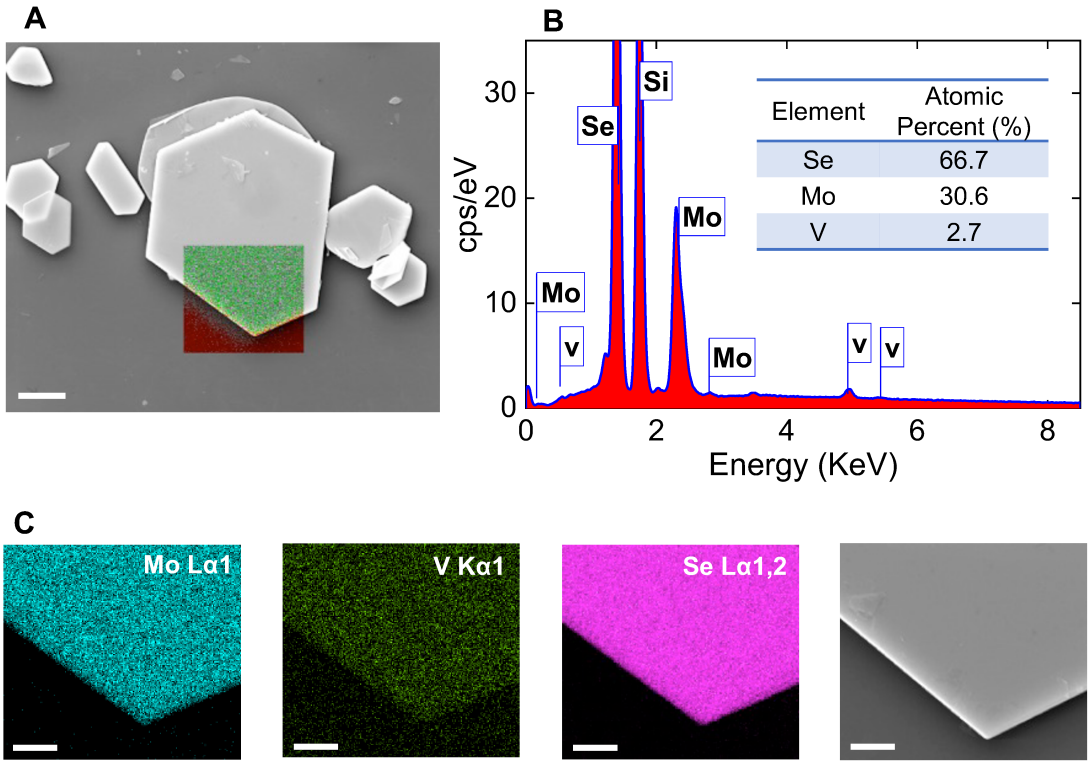

Figure S23. SEM-EDX characterization of $Mo_{1-x}V_xSe_2$ sample. (A) SEM image of the $Mo_{1-x}V_xSe_2$ flake (scale bar: 4 μm). **(B)** EDX spectrum acquired from the area marked by a square in **(A).** The quantification results are presented in the table, showing the average stoichiometry ratio of $Mo_{0.91}V_{0.08}Se_2$. **(C)** Full EDX composition mapping of the detected elements (scale bars: 2 μm).

S5. Raman spectroscopy characterization

Comparison of the Raman spectra of NbS_2, $NbSe_2$, TaS_2, $TaSe_2$, WS_2 and their alloyed structures are presented in Figure S24. The Raman spectra are shifted vertically for clarity. For the $Nb_{1-x}Ta_xS_2$ alloy (x = 0.5), the Raman spectra contain modes at 79, 285, 302, 383 cm^{-1} corresponding to A_{1g}^2, E_{2g}^1, E_g^2, A_g^1, respectively.[1–7] For the $Nb_{1-x}Ta_xSe_2$ alloy (x = 0.5), the Raman spectra contain peaks at 135, 232, and 254 cm^{-1} corresponding to E_{1g}, A_{1g}, and E_{2g},

respectively. Also spectra of $W_{1-x}Nb_xS_2$ (x = 0.5) indicate Raman modes at 287, 320, 354, 390, 410 cm^{-1}, which corresponds to E_g^1, E_g^2, E_{2g}^1, A_g^1, A_{1g}, respectively.[8,9]

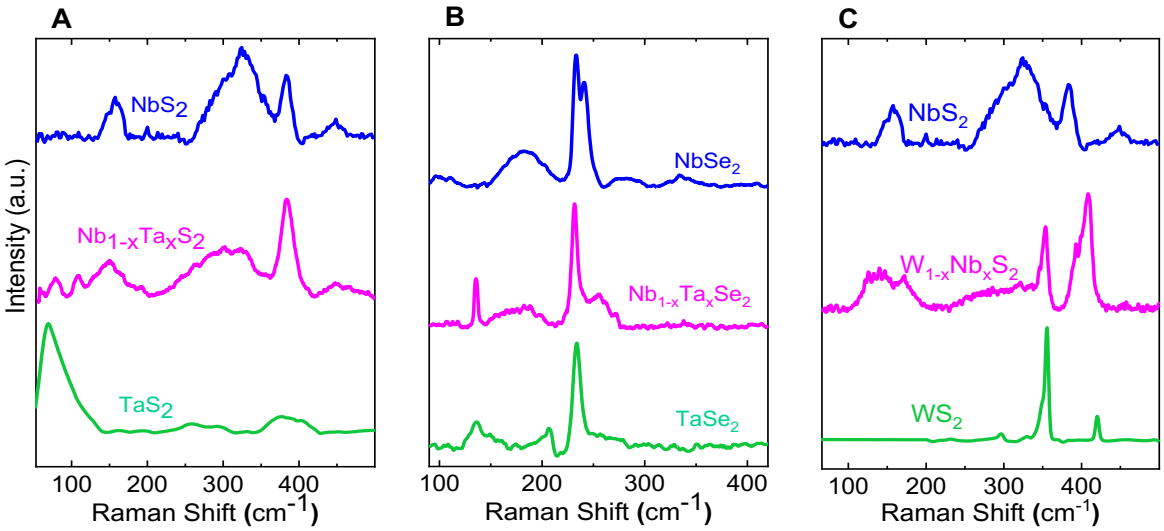

Figure S24. Raman characteristics of binary alloys at ambient conditions excited by 532 nm excitation laser. (A) Comparison of the Raman spectra of NbS_2, TaS_2, and $Nb_{1-x}Ta_xS_2$ alloy. **(B)** Comparison of the Raman spectra of $NbSe_2$, $TaSe_2$, and $Nb_{1-x}Ta_xSe_2$ alloy. **(C)** Comparison of the Raman spectra of NbS_2, WS_2, and $W_{1-x}Nb_xS_2$ alloy. Raman spectra are shifted vertically for clarity.

S6. X-ray photoelectron spectroscopy (XPS)

Figure S25 represents the XPS spectra obtained for 3 representative alloys. All the spectra were calibrated based on the C-C bond energy at 284.8 eV. The major Nb core levels of $Nb_{1-x}Ta_xS_2$ were observed at ~203.7 and ~206.4 eV, corresponding to $Nb3d_{5/2}$ (Figure S25A). The Ta4f spectrum in Figure S25B shows two distinct peaks at ~23.5 and ~25.4 eV, representing $Ta4f_{7/2}$ and $Ta4f_{5/2}$, respectively. Figure S25C indicates the S 2p region, including two main peaks located at ~161 and ~162.4 eV corresponding to $S2p_{3/2}$ and $S2p_{1/2}$. For $Nb_{1-x}Ta_xSe_2$, the Nb region is shown in Figure S25D with Nb core level peaks located at ~203.3 and ~206 eV which represent $Nb3d_{5/2}$.

Two high-intensity peaks of Ta4f spectrum is also observed at ~22.7 and ~24.7 eV associated with $Ta4f_{7/2}$ and $Ta4f_{5/2}$, respectively. Se 3d region in $Nb_{1-x}Ta_xSe_2$ indicates the main peaks at ~53.6 and ~55.2 eV representing $Se3d_{5/2}$ and $Se3d_{3/2}$. $W_{1-x}Nb_xS_2$ XPS results include two distinct peaks of $Nb3d_{5/2}$ located at ~202 and ~205.5 eV. W4f region shows the major peaks of $W4f_{7/2}$ and $W4f_{5/2}$ at ~31.2 and ~33.3 eV. S2p region in $W_{1-x}Nb_xS_2$ indicates two peaks at ~160.5 and ~161.8 eV corresponding $S2p_{3/2}$ and $S2p_{1/2}$ (Figure S25G-I).[9]

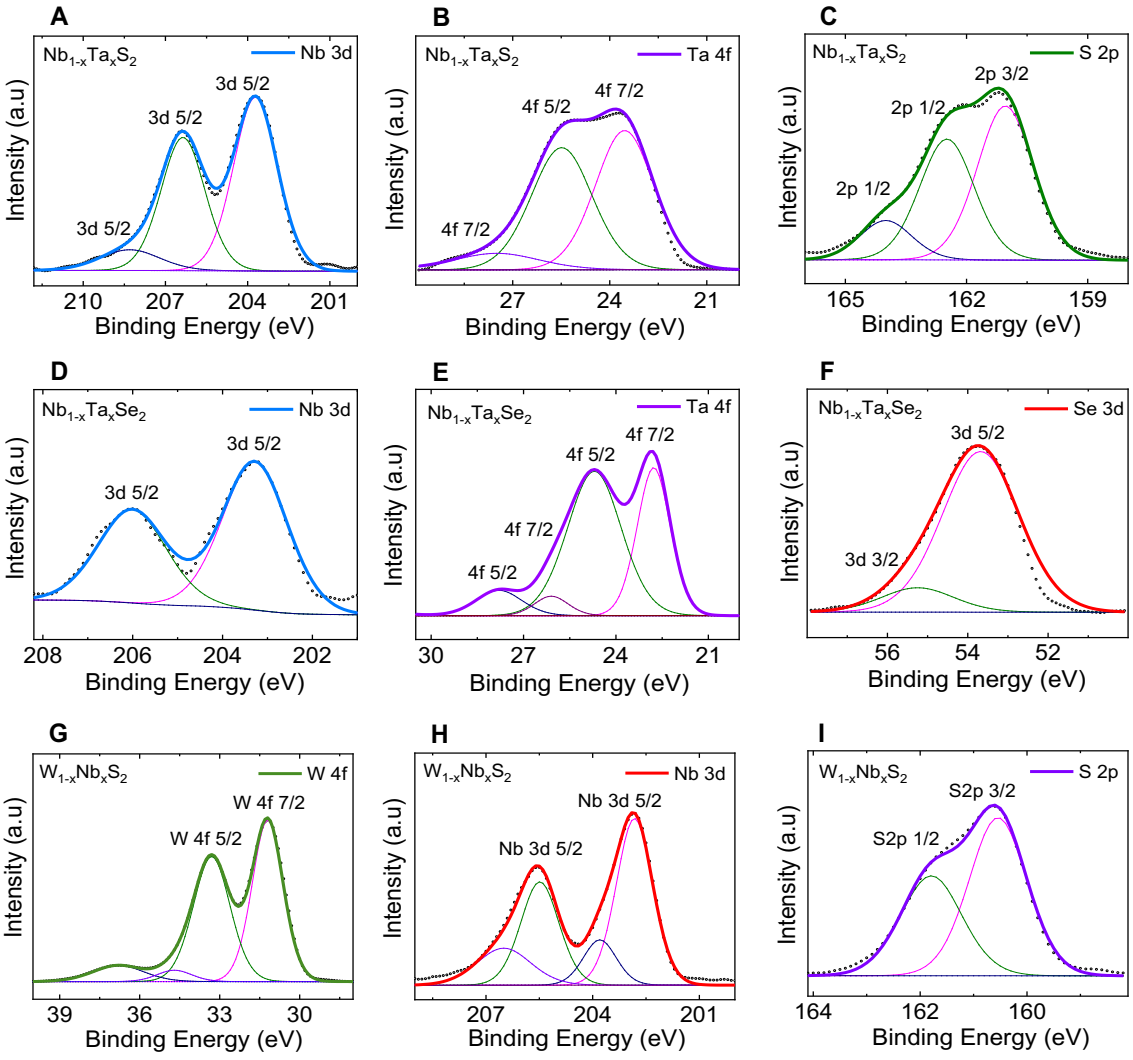

Figure S25. XPS spectra of the synthesized binary alloys. (A-C) XPS spectra of the Nb 3d, Ta 4f, and S 2p core level peaks for the $Nb_{1-x}Ta_xS_2$ alloy. **(D-F)** XPS spectra of the Nb 3d, Ta 4f, and Se 3d core level peaks for the $Nb_{1-x}Ta_xSe_2$ alloy. **(G-I)** XPS spectra of the W 4f, Nb 3d, and S 2p core level peaks for the $W_{1-x}Nb_xS_2$ alloy. The binding energy of C-C bonding is set at 284.8 eV.

S7. X-ray diffraction spectroscopy (XRD)

To determine the crystallinity of the three representative alloys ($Nb_{1-x}Ta_xS_2$, $Nb_{1-x}Ta_xSe_2$, and $W_{1-x}Nb_xS_2$), X-ray diffraction (XRD) experiment was performed (Figure S26). The samples were mechanically exfoliated and transferred to XRD wafer for the measurement. The materials are in hexagonal symmetry with the diffraction pattern similar to their pure single metal chalcogenides preferentially oriented along (001) direction.[10–15] The sharp peaks recorded suggest that the materials are highly crystalline.

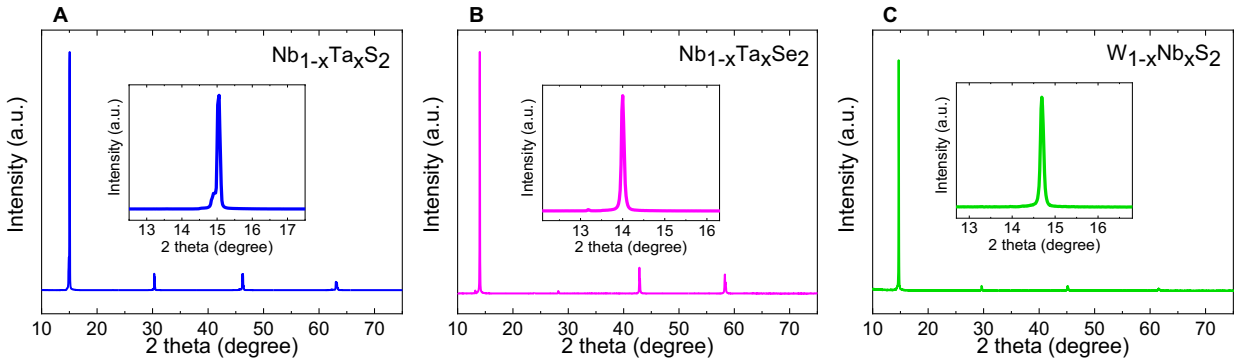

Figure S26. XRD patterns obtained from binary alloys of (A) $Nb_{1-x}Ta_xS_2$, (B) $Nb_{1-x}Ta_xSe_2$, and (C) $W_{1-x}Nb_xS_2$ at ambient conditions.

S8. Thermogravimetric analysis (TGA) characterization

To compare the thermal stability of the $Nb_{1-x}Ta_xS_2$ alloy and NbS_2, we performed EDX and XPS measurements, after the TGA experiments. Figure S28 represent the SEM-EDX characterization for the $Nb_{1-x}Ta_xS_2$ alloy after TGA experiment, which verifies the stability of all the elements. Moreover, SEM images confirm that flakes retain their layered morphology after TGA test at elevated temperatures. However, for the NbS_2 sample, EDX data show that sulfur completely evaporated at elevated temperatures (Figure S29). Comparison of the XPS data before and after the TGA test for the NbS_2 sample also verify the sulfur evaporation (Figure S30). The

optical image for the NbS_2 powder shows that the powder's color changes after heating up to 1230 K, while this is not the case for $Nb_{1-x}Ta_xS_2$ alloy (Figure S31).

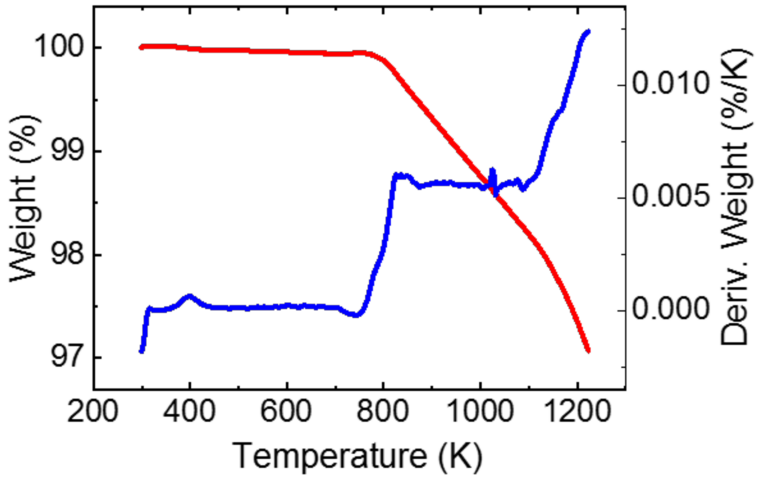

Figure S27. Thermogravimetric analysis (TGA) characterization of $Nb_{1-x}Ta_xS_2$ sample. Showing only 3 weight % loss of material due to volatile escapes starting from ~780K.

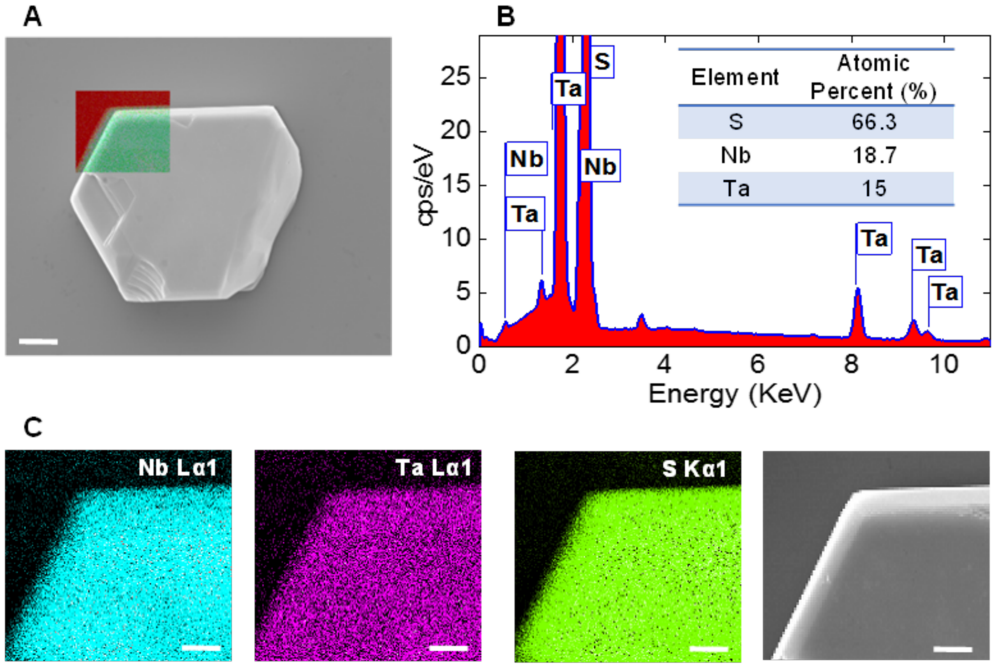

Figure S28. SEM-EDX characterization of $Nb_{1-x}Ta_xS_2$ sample after TGA. (A) SEM image of the $Nb_{1-x}Ta_xS_2$ flake (scale bar: 4 μm). **(B)** EDX spectrum acquired from the area marked by a square in **(A).** The quantification results are presented in the table, showing the average

stoichiometry ratio of $Nb_{0.55}Ta_{0.45}S_2$. **(C)** Full EDX composition mapping of the detected elements (scale bars: 2.5 μm).

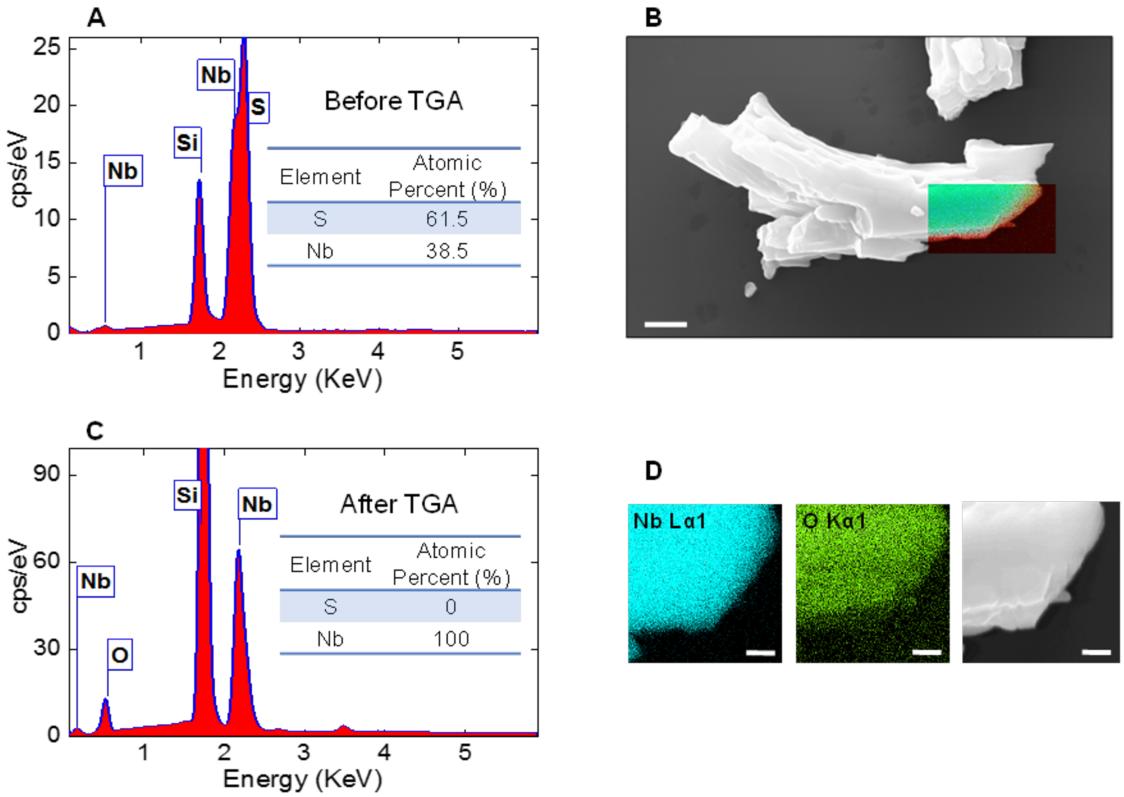

Figure S29. SEM-EDX characterization of NbS_2 sample before and after TGA. (A) EDX spectrum acquired from NbS_2 sample before TGA measurements. **(B)** SEM image of the NbS_2 flake after TGA measurements at elevated temperatures up to 1230 K. (scale bar: 1 μm). **(C)** EDX spectrum acquired from the area marked by the square in **(B)**. **(D)** Full EDX composition mapping of the detected elements (scale bars: 500 nm).

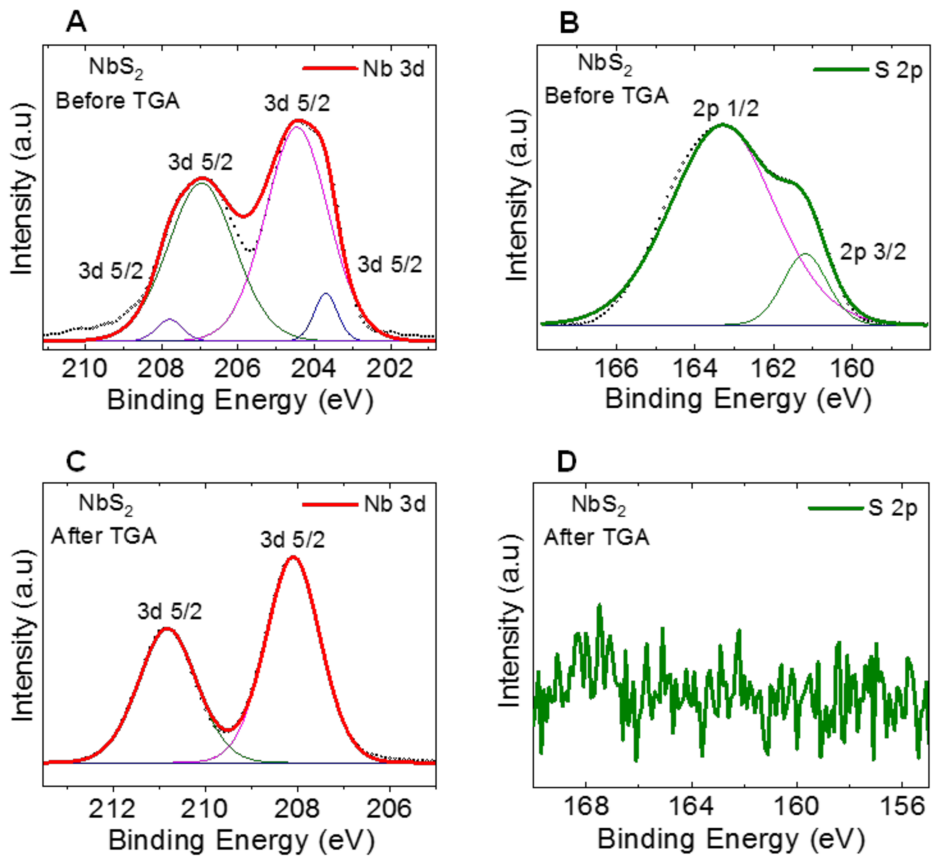

Figure S30. XPS spectra of the NbS_2 sample before and after TGA. (A, B) XPS spectra of the Nb 3d, and S 2p core level peaks for the NbS_2 sample before TGA. **(C, D)** XPS spectra of the Nb 3d, and S 2p core level peaks for the NbS_2 sample after TGA.

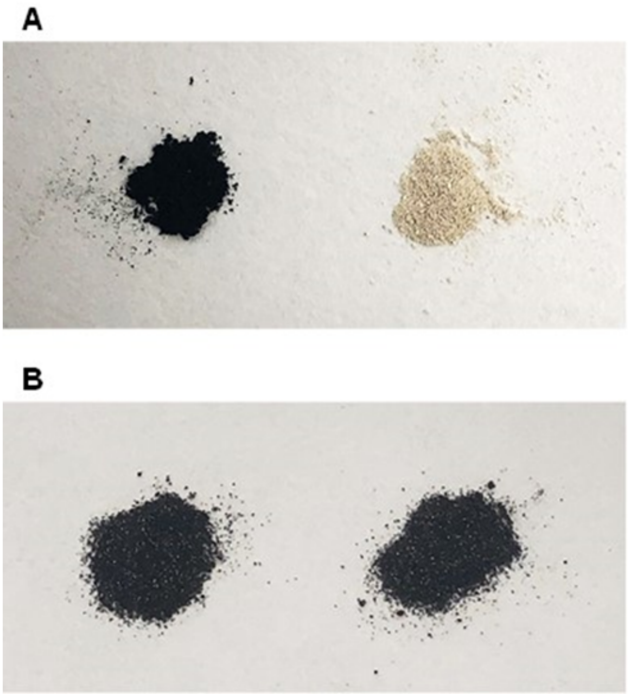

Figure S31. Powder optical images before and after TGA. (A) Optical image of NbS_2 powder before and after TGA showing color change due to the sulfur evaporation. **(B)** Optical image of $Nb_{1-x}Ta_xS_2$ powder before and after TGA verifying its thermal stability at elevated temperatures.

S9. DLS and AFM characterization of Nano-flakes (NFs)

As-synthesized TMDC alloy NFs dispersed in IPA were used for DLS experiments. The obtained average lateral sizes of $Nb_{1-x}Ta_xS_2$, $Nb_{1-x}Ta_xSe_2$, and $W_{1-x}Nb_xS_2$ NFs were ~222 nm, ~199nm and ~130nm, respectively (Figure S32A-C). Atomic force microscopy (AFM) technique was then employed to image the surface morphology and determine the thickness distributions of the exfoliated NFs. For this purpose, the supernatant decanted from the centrifuge was drop-cast onto a SiO_2/Si (~300 nm/0.5 mm) substrate for AFM imaging. Figure S32D-F show AFM height profile distribution of the exfoliated materials obtained from ~50 randomly selected exfoliated flakes. AFM imaging of individual flakes displays typical thicknesses of ~8 to 22 nm for the synthesized NFs (Figure S32G-I).

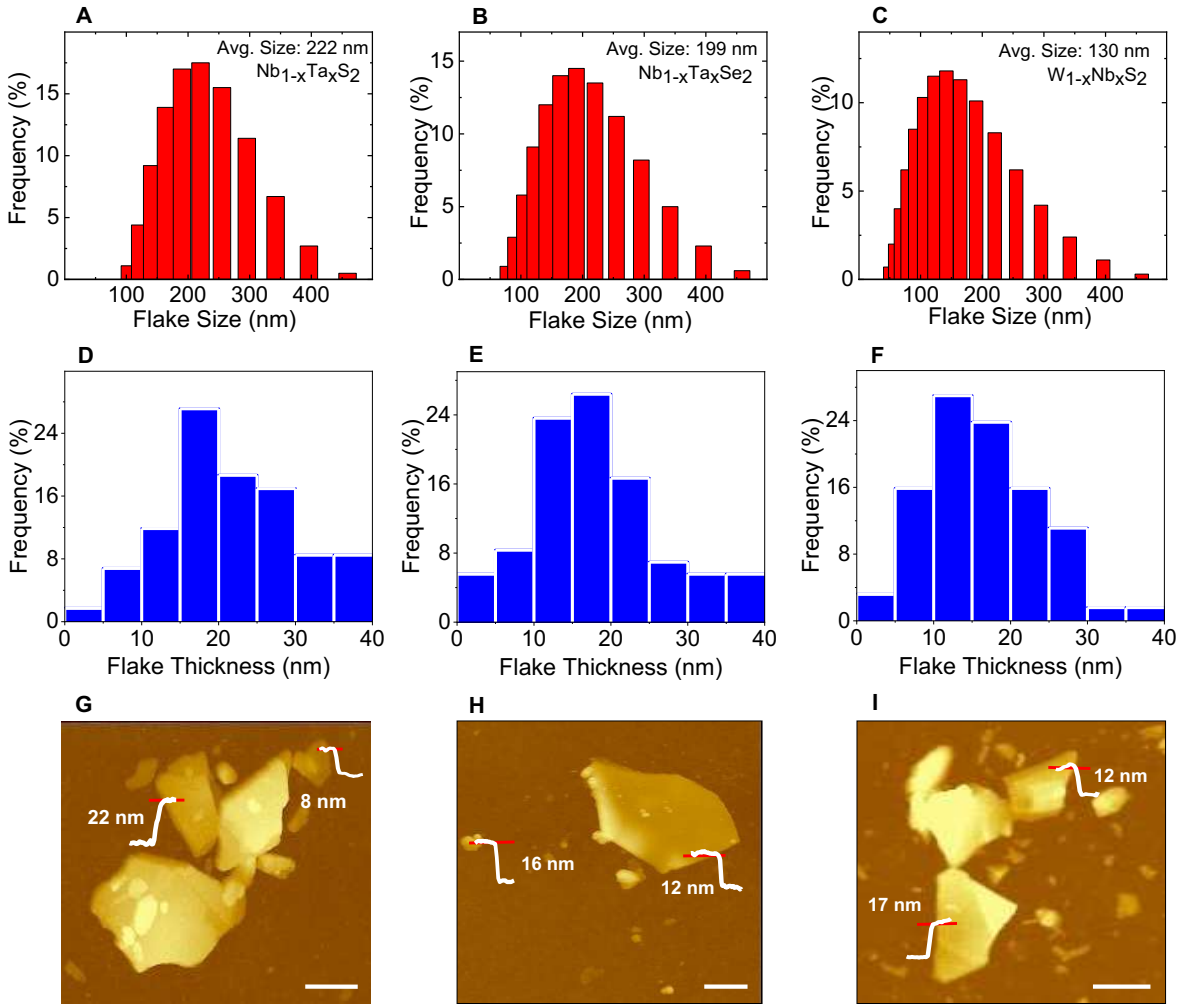

Figure S32. DLS and AFM characterization of nano-flakes. (A-C) Size distribution from DLS measurements on 40 flakes for binary alloys of $Nb_{1-x}Ta_xS_2$, $Nb_{1-x}Ta_xSe_2$, and $W_{1-x}Nb_xS_2$, respectively. **(D-F)** Frequency distribution of flake thickness obtained by AFM measurements on ~50 randomly selected exfoliated flakes for binary alloys of $Nb_{1-x}Ta_xS_2$, $Nb_{1-x}Ta_xSe_2$, and $W_{1-x}Nb_xS_2$, respectively. **(G-I)** Typical AFM image of individual liquid-exfoliated nano-flakes (Scale bar is 200 nm).

S10. Ultraviolet Photoelectron Spectroscopy (UPS)

The work function for synthesized binary TMDCs alloys and MoS_2 was measured by using ultraviolet photoelectron spectroscopy (UPS). In the UPS experiment, a bias of -10 V was applied to the sample to differentiate the sample energy cut-off from that of the spectrometer. Silver was

used as a reference for the calibration based on the metal Fermi edge.[9] In the next step, UPS measurements were performed for the synthesized bulk alloys, and the obtained spectra were shifted according to silver's calibration data. The work function values were calculated based on the equation φ_{TMDC}= hν-Ec. hν is the exciting photon energy of the ionization source (He I) which is 21.2 eV. Ec is the binding energy of secondary edge cut-off referring to lower kinetic energy.[16] The work function values were measured for three points on each sample to obtain the error bars. The work function values and the error bars for three different measurements are shown in Figure S33 compared to the work function of MoS_2.

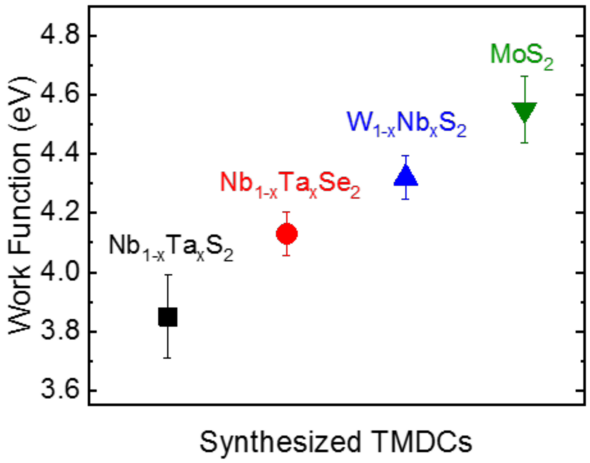

Figure S33: Ultraviolet Photoelectron Spectroscopy (UPS) results for the selected synthesized alloys.

S11. Three-Electrode Cell for Electrochemical CO_2 reduction experiment

All chemicals were reagent grade and were used as-received without additional purification. Choline chloride ($C_5H_{14}CINO$) was purchased from Sigma-Aldrich. Potassium hydroxide (KOH) was purchased from Fisher-Scientific. Carbon dioxide (CO_2) was purchased from Praxair. Solutions were prepared using Barnstead NANO pure water (18.2 MΩ and 25°C). Figure S34 shows LSV results for three tested alloy materials.

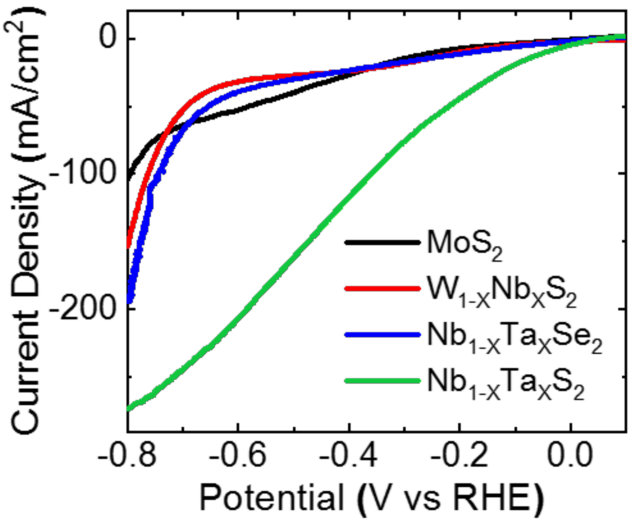

Figure S34: Linear Sweep Voltammetry (LSV) results for electrochemical reduction of CO_2 in 1 M choline chloride and 1 M potassium hydroxide using $Nb_{1-x}Ta_xS_2$ (green), $Nb_{1-x}Ta_xSe_2$ (blue), $W_{1-x}Nb_xS_2$ (red) and MoS_2 (black) at scan rate of 1 $mV.s^{-1}$.

S12. SEM and Raman spectroscopy characterization of cathode

To explore the surface structure and morphology of $Nb_{1-x}Ta_xS_2$ NFs, SEM characterization was carried out. Figure S35A shows the surface of the cathode after 10th discharge process. The blurry and cloudy like products are attributed to Li_2O_2 products which are homogeneously covered the active material. Subsequently, during the 10th charge process (Figure S35B), Li_2O_2 is decomposed and surface is only covered by $Nb_{1-x}Ta_xS_2$ active catalyst.

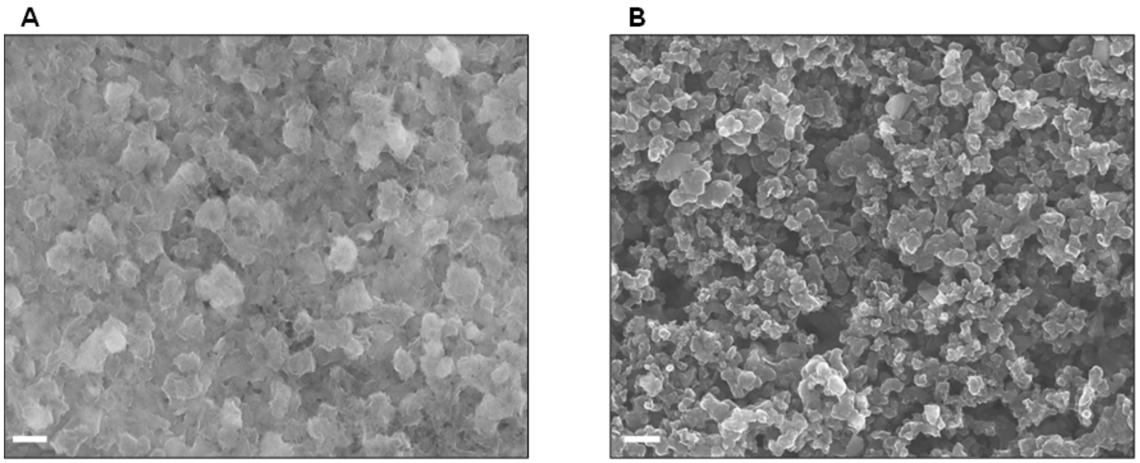

Figure S35. Scanning Electron Microscopy (SEM) images of cathode after 10th discharge (A) and 10th charge (B) (Scale bar is 200 nm).

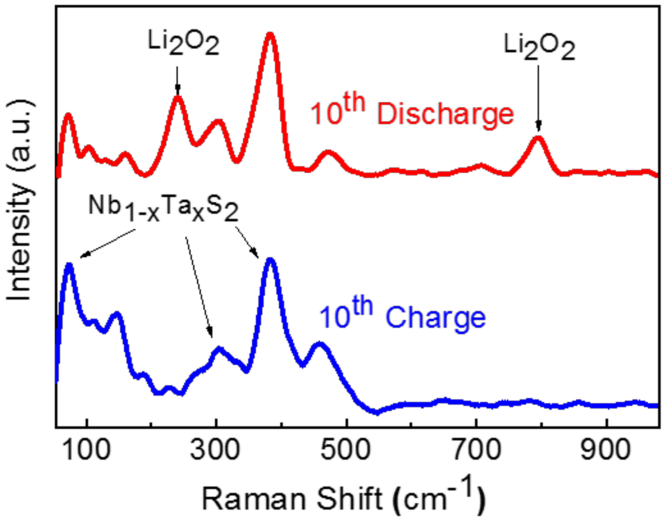

Figure S36. Raman spectroscopy characterization of cathode after 10th discharge and charge processes. Peaks located at 246 and 788 cm^{-1} are associated with Li_2O_2 formed during discharge. The presence of other peaks are due to the catalyst and substrate.

S13. Electrical current-voltage (I-V) characteristics of devices

To characterize the electrical performance of the synthesized alloys, the $Nb_{1-x}Ta_xS_2$ nanoflakes (NFs) were produced through mechanical exfoliation technique (Figure S37). To

examine the current-voltage (I-V) characteristics of $Nb_{1-x}Ta_xS_2$ devices, few-layer, tape-exfoliated flakes were transferred onto a SiO_2/Si (~300 nm/0.5 mm) substrate. By using an optical microscope (OM) and AFM, uniform and thin flakes were selected for subsequent experiments. The samples were quickly spin-coated with a layer of poly (methyl methacrylate) (PMMA) which serves both as a protective layer and a resist for electron beam lithography (EBL) technique. The contact electrodes were then predefined and patterned in a two- and four-probe configurations with standard photolithography techniques. After patterning, we fabricated the metal electrodes by deposition of Cr/Au (5/50 nm) via electron-beam evaporation process followed by a lift-off process in acetone. Figure S38 demonstartes the current versus applied voltage (I_{DS}-V_{DS}) with zero gate voltage in the 50–295 K temperature range. Transport measurements verify Ohmic contacts were formed. We also observed a negligible gate dependency in room-temperature transfer curves (I_{DS}–V_G). Inset of Figure S38 shows the AFM image of a typical tested device.

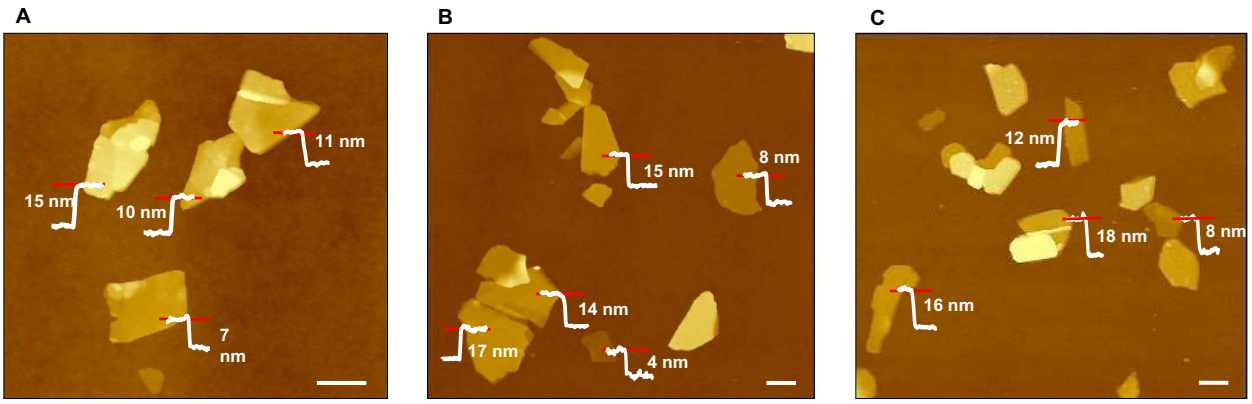

Figure S37: AFM characterization of mechanical exfoliated nano-flakes. (A-C) Typical AFM images of individual micro mechanically exfoliated nano-flakes for binary alloys of $Nb_{1-x}Ta_xS_2$, $Nb_{1-x}Ta_xSe_2$, and $W_{1-x}Nb_xS_2$, respectively (Scale bar is 200 nm).

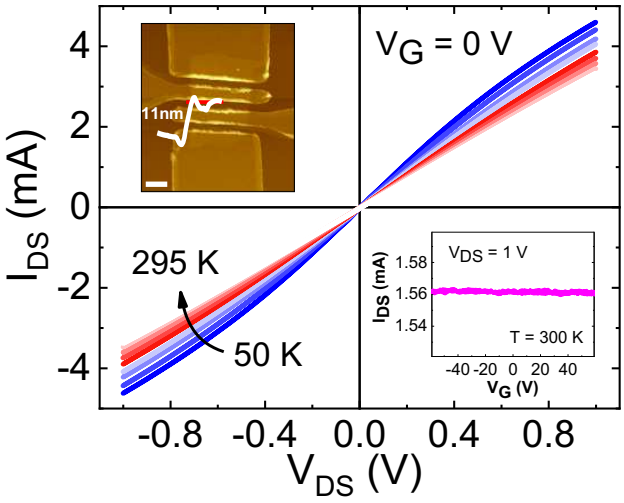

Figure S38: Electrical current-voltage (I-V) characteristics of $Nb_{1-x}Ta_xS_2$ devices. Temperature-dependent current-voltage (I_{DS}-V_{DS}) transport characteristics of a representative device at zero gate voltage. Upper left inset shows the AFM micrograph of a tested device (Scale bar is 2 µm). Lower inset shows the room-temperature current-voltage (I_{DS}-V_G) transfer characteristics from -60 to +60 V gate potential at V_{DS} = 1 V.

References:

[1] M. Staiger, V. Bačić, R. Gillen, G. Radovsky, K. Gartsman, R. Tenne, T. Heine, J. Maultzsch, C. Thomsen, *Phys. Rev. B* **2016**, *94*, 1.

[2] S. Zhao, T. Hotta, T. Koretsune, K. Watanabe, T. Taniguchi, K. Sugawara, T. Takahashi, H. Shinohara, R. Kitaura, *2D Mater.* **2016**, *3*, 25027.

[3] R. Zhao, B. Grisafe, R. K. Ghosh, K. Wang, S. Datta, J. Robinson, *Nanoscale* **2019**, *11*, 6016.

[4] O. R. Albertini, R. Zhao, R. L. McCann, S. Feng, M. Terrones, J. K. Freericks, J. A. Robinson, A. Y. Liu, *Phys. Rev. B* **2016**, *93*, 1.

[5] Q. Hu, C. Yin, L. Zhang, L. Lei, Z. Wang, Z. Chen, J. Tang, R. Ang, *Chinese Phys. B* **2018**, *27*.

[6] A. Dankert, M. Venkata Kamalakar, A. Wajid, R. S. Patel, S. P. Dash, *Nano Res.* **2015**, *8*, 1357.

[7] R. Zhao, B. Grisafe, R. K. Ghosh, S. Holoviak, B. Wang, K. Wang, N. Briggs, A. Haque, S. Datta, J. Robinson, *2D Mater.* **2018**, *5*, 25001.

[8] J. Zhou, J. Lin, X. Huang, Y. Zhou, Y. Chen, J. Xia, H. Wang, Y. Xie, H. Yu, J. Lei, D. Wu, F. Liu, Q. Fu, Q. Zeng, C.-H. Hsu, C. Yang, L. Lu, T. Yu, Z. Shen, H. Lin, B. I. Yakobson, Q. Liu, K. Suenaga, G. Liu, Z. Liu, *Nature* **2018**, *556*, 355.

[9] L. Majidi, P. Yasaei, R. E. Warburton, S. Fuladi, J. Cavin, X. Hu, Z. Hemmat, S. B. Cho, P. Abbasi, M. Vörös, L. Cheng, B. Sayahpour, I. L. Bolotin, P. Zapol, J. Greeley, R. F. Klie, R. Mishra, F. Khalili-Araghi, L. A. Curtiss, A. Salehi-Khojin, *Adv. Mater.* **2019**, *31*, 1804453.

[10] Y. H. Huang, C. C. Peng, R. S. Chen, Y. S. Huang, C. H. Ho, *Appl. Phys. Lett.* **2014**, *105*, 93106.

[11] L. Najafi, S. Bellani, R. Oropesa-Nuñez, B. Martín-García, M. Prato, V. Mazánek, D. Debellis, S. Lauciello, R. Brescia, Z. Sofer, F. Bonaccorso, *J. Mater. Chem. A* **2019**, *7*, 25593.

[12] Y. H. Huang, R. S. Chen, J. R. Zhang, Y. S. Huang, *Nanoscale* **2015**, *7*, 18964.

[13] Z. Yan, C. Jiang, T. R. Pope, C. F. Tsang, J. L. Stickney, P. Goli, J. Renteria, T. T. Salguero, A. A. Balandin, *J. Appl. Phys.* **2013**, *114*, 204301.

[14] M. A. Ibrahem, T. Lan, J. K. Huang, Y.-Y. Chen, K.-H. Wei, L.-J. Li, C. W. Chu, *RSC Adv.* **2013**, *3*, 13193.

[15] H. Enomoto, T. Kawano, M. Kawaguchi, Y. Takano, K. Sekizawa, *Jpn. J. Appl. Phys.* **2004**, *43*, L123.

[16] R. Schlaf, H. Murata, Z. H. Kafafi, *J. Electron Spectros. Relat. Phenomena* **2001**, *120*, 149.